Influence of tectonic and geological structure on GIC in southern South Island, New Zealand

M. Ingham[1], K. Pratscher[1], W. Heise[2], E. Bertrand[2], M. Kruglyakov[3], C.J. Rodger[3]

[1]School of Chemical and Physical Sciences, Victoria University of Wellington, Wellington, New Zealand.

[2]GNS Science, Lower Hutt, New Zealand.

[3]Department of Physics, University of Otago, Dunedin, New Zealand.

Corresponding author: Malcolm Ingham (malcolm.ingham@vuw.ac.nz)

Key Points:

- Magnetotelluric measurements have ben made at 62 sites across southern South Island, New Zealand
- MT impedance tensors are used to calculate the induced electric fields resulting from a 100 nT variation in magnetic field
- A simplified representation of the transmission network is used to assess how enhanced/reduced fields associated with particular tectonic features influence calculated GIC

Abstract

As part of a 5-year project to assess the risk posed by geomagnetically induced currents (GIC) to the New Zealand electrical transmission network, long-period magnetotelluric (MT) measurements have been made at 62 sites in southern South Island of New Zealand, a region where there was an absence of previous MT data. The data are largely 3-dimensional in character, but show distinct features that can be related to the known tectonic and geological structure. In this work we focus on how the measured MT impedance tensors, and a simple interpretation of conductivity structure, can be used to assess the influence of tectonic and geological structure on GIC. We use the impedance tensors to calculate the magnitudes and orientations of induced electric fields in response to various orientations of inducing magnetic field. The electric fields so calculated are then used in a simplified model of the transmission network to calculate GIC at grounded substations. Our results confirm that tectonic/geological structure in the lower South Island and the resulting electrical conductivity variations have important impacts on the GIC magnitude. In the south-west, smaller induced electric fields, associated with the higher conductivity in that region, lead to much reduced GIC at a substation in that area. In contrast, higher electric fields occurring in a NW-SE band across the centre of the region, contribute to much larger GIC in Dunedin city. Our results thus help explain the observed GIC reported at transformers in the region.

Plain Language Summary

Variations in the Earth's magnetic field during magnetic storms produce induced currents in the ground which in certain circumstances may present a risk to an electricity transmission network. Understanding the risk in any given region requires knowledge of the local ground electrical conductivity structure. To help map the structure across southern South Island, New Zealand, we have made long period magnetotelluric measurements made at 62 sites. We use these measurements to calculate the electric fields which would be induced in the ground due to magnetic field variations. Using a simplified representation of the electrical transmission network, we use these calculated electric fields to assess how particular features of the geological structure influence the currents (geomagnetically induced currents – GIC) that can be produced in the power network.

1 Introduction

Over the last decade considerable research has focused on the risk that geomagnetically induced currents (GIC) present to electrical transmission networks (e.g. Bailey et al., 2017, 2018; Beggan et al., 2013; Blake et al., 2016; Campanaya et al., 2019; Kelbert & Lucas, 2020; Love et al., 2018a, 2018b; Mylss et al., 2014; Torta et al., 2017; Watari et al. 2021, Wik et al., 2009). The risk due to GIC depends on the distribution of induced electric fields during a geomagnetic storm. Although the induced fields are linearly related to the rate of change of the magnetic field (e.g. Viljanen, 1997; Viljanen et al., 2001; Dimmock et al., 2020), they are also highly influenced by local or regional ground conductivity structure (e.g. Viljanen & Pirjola, 2017; Love et al., 2018a, 2018b). Understanding how induced electric fields depend on the regional tectonic and geological structure can give key insights into why the observed magnitude of GIC may vary from location to location.

In recent years there has been considerable research into the hazard presented by GIC to the New Zealand electrical transmission network (Divett et al., 2017, 2018, 2020; Ingham et al., 2017; Mac Manus et al., 2022a; Mukhtar et al., 2020). Due to closer proximity to the auroral zone, the risk is perceived to be highest in the South Island of New Zealand, where Transpower New Zealand, the transmission line operator, has been monitoring GIC for over 2 decades. One of the methods for mapping variations in both the magnitude and orientation of induced electric fields across a region is to calculate them directly from the magnetic field spectrum for a specified geomagnetic storm using magnetotelluric (MT) impedance tensors from a two-dimensional distribution of sites. Prior to 2020, MT sites in the South Island have largely been limited to transects of sites across the northern and central parts of the Island (Ingham 1996; Wannamaker et al., 2002, 2009) making the use of MT data in assessing GIC risk impractical. As a step to improving coverage of MT data, an extensive long period MT survey across Otago and Southland in the southern part of the South Island of New Zealand has recently been completed. Full details of analysis and inversion modelling of this data to reveal details of the lithospheric conductivity structure will be described in a future publication. In this paper we focus on how the measured MT impedance tensors, and a simple interpretation of conductivity structure, can be used to assess the influence of tectonic and geological structure on GIC in the southern part of the South Island of New Zealand.

We start by discussing the tectonic and geological framework of the study area and the extent of the MT data survey. We then use apparent resistivity and phases calculated from the determinant impedance to give a broad picture of conductivity variations across the area. We use the impedance tensors to calculate the magnitudes and orientations of induced electric fields in response to various orientations of a uniform inducing magnetic field. The calculated electric fields are then used in a simplified electrical model of the transmission network in the region to calculate GIC at grounded substations. By replacing anomalously large or small geolectric fields associated with prominent tectonic/geological features with more uniform values, we assess how the tectonic/geological structure influences calculated GIC. Carried out in the frequency domain, our analysis differs from that employed by Bedrosian & Love (2015) who used impedance tensors measured as part of the Earthscope

program to map the time variation of induced electric fields across the mid-western United States, and related the magnitude of the induced fields to the underlying conductivity structure. Similar investigations were also performed for the north of England and southern Scotland by Mackay & Whaler (2006), who also looked at the influence of galvanic distortion on the orientation and magnitude of electric fields, by Nakamura et al. (2018) in a study of GIC in the Japanese 500-kV power grid, and by Marshalko et al. (2020) for the eastern United States.

2 Geological/tectonic setting and previous geophysical measurements

New Zealand lies on the boundary between the Australian and Pacific tectonic plates. Throughout the South Island this boundary is marked by the Alpine Fault, a transform fault which, over the last 25 Myr, has seen about 480 km of lateral movement. The convergence of the Pacific and Australian plates along the fault has led to the uplift of the Southern Alps along the central part of the South Island. The geological structure of the study area (shown in Figure 1) reflects both this movement and the complex history of accretion of terranes and periodic rifting events (King, 2000) at the margin of Gondwana from around 300 Myr (Sutherland et al., 2000). As a result, as described by Mortimer et al. (2012), the basement across the study area is made up of a “collage” of volcano-sedimentary terranes of which some have been affected by metamorphism and/or intrusion.

From the west coast of Fiordland to Invercargill and the Hollyford Fault the basement consists of the 250-100 Myr Median Batholith and the adjacent Brook Street Terrane. Both represent volcanic arcs generated behind subduction zones. East of these features, the Murihiku Terrane is composed primarily of sandstones and siltstones, and is bounded on its north-east by the Foothills Fault which delineates the south-western boundary of the Dun Mountain – Matai Terrane. The Dun Mountain – Matai Terrane is covered by Cenozoic and Cretaceous sediments along much of its length and consists of obducted oceanic crust (the Dun Mountain Ophiolite Belt) overlain by continental margin sandstones and limestones. The Dun Mountain Ophiolite Belt (DMOB) can be traced for about 1000 km into the North Island through the Stokes Magnetic Anomaly (Hunt, 1978). To the north are Permian and Triassic greywackes which over a large part of the area have been metamorphically altered to schist (the Haast schist) which is comprised of fault controlled north-east trending parallel ridges and basins (Ballance, 2009).

The majority of the study area is overlain by Cenozoic and Cretaceous sedimentary deposits, river gravels and alluvium. The sediments are thickest across the eastern portion of the Median Batholith between Fiordland and the western edge of Southland, in a region known as the Moonlight Tectonic Zone - MTZ - (Ballance, 2009). This marks the location of a spreading centre between the Pacific and Australian tectonic plates, active between 45-25 Myr (King, 2000). The only recent volcanism in the study area is related to the 13-10 Myr Dunedin volcano, the remnants of which now make up the Dunedin peninsula and are unrelated to the accretionary and rifting events.

The Alpine Fault passes off-land in the north-west of the study area and immediately to the south-west of the lower South Island the Australian Plate subducts steeply under the Pacific Plate at the Puysegur Trench.

3 Magnetotelluric measurements

Long period magnetotellurics (MT) is a passive geophysical method that incorporates a cartesian layout of two electric dipoles and a fluxgate magnetometer to record Earth's naturally occurring electric and magnetic fields. These measurements are used to calculate an impedance tensor relating variations in the induced electric field to those in the magnetic field. The impedance tensor $\underline{\underline{Z}}$ has components Z_{xx}, Z_{xy}, Z_{yx} and Z_{yy} and relates the induced horizontal components of the electric field to the variations in the horizontal components of the magnetic field through

$$E_x = (Z_{xx}B_x + Z_{xy}B_y)/\mu_0 \quad (1)$$

$$E_y = (Z_{yx}B_x + Z_{yy}B_y)/\mu_0 \quad (2)$$

$\underline{\underline{Z}}$ is a function of frequency and depends upon the electrical conductivity structure of the earth. Long period MT refers to data acquisition within the frequency range of .0001 to 1 Hz, for which the source signal originates from the interaction of the solar wind with the geomagnetic field.

The locations of 62 long period magnetotelluric sites across Otago and Southland are shown in Figure 1. The MT measurements were made using LEMI-417M instrumentation produced by the Lviv Centre of the Institute for Space Research, Ukraine, utilizing fluxgate magnetometers with a frequency band from 0.3 - 10^{-5} Hz, and $Pb/PbCl_2$ electrodes constructed in-house by GNS Science. Measurements were made over a period of 15 months from February 2021 to May 2022, with eight sites at a time operating simultaneously with a remote reference site situated in the centre of the North Island. At each site data were recorded for approximately 1 month with a sampling interval of 1 second. Data quality was generally good with the exception of three sites where electric or magnetic field cables were disturbed by wildlife. Impedance tensor estimates were calculated, in geographic coordinates (x-axis oriented to north, y to east) in the period range from 5-100000 seconds. Examples of the calculated impedances, which are of good quality in the range 10-10000 seconds, albeit with increased scatter and uncertainty outside this range, are shown in Figure 2.

Analysis both of phase tensors (Caldwell et al., 2004; Bibby et al., 2005) and of dimensionality indices (Weaver et al., 2000; Marti et al., 2009) suggest that the overall electrical conductivity structure of this part of the South Island is, as might be expected from the tectonics, highly complex, and will require 3-dimensional numerical modelling/inversion. As our interest in the present paper is to analyse the effects of tectonic/geological structure on induced electric fields, and hence GIC, we use pseudosections of the so-called determinant apparent resistivity and phase measurements to gain an initial understanding of the principal features of the conductivity structure.

4 Determinant apparent resistivity and phase

Although, as indicated above, complete understanding of the conductivity structure associated with the study area requires full 3-dimensional inversion modelling, some simpler methods of gaining an insight into the principal structural features are available. In particular the use of parameters which are derived from the magnetotelluric impedance tensor and are invariant upon rotation suggest the possibility of assessing the variation in conductivity structure with depth beneath a site. Ingham (1988) investigated the use of the apparent resistivity and phase calculated from the determinant impedance defined by

$$Z_{det} = \sqrt{Z_{xx}Z_{yy} - Z_{xy}Z_{yx}} \quad (3)$$

which has the advantage of being a function of all four elements of the impedance tensor. If the true impedance tensor is affected by galvanic distortion through a real distortion tensor $D = \begin{pmatrix} a & b \\ c & d \end{pmatrix}$ then the measured determinant is related to it only through a multiplicative constant $\sqrt{ad - bc}$. Hence the determinant phase is unaffected and the apparent resistivity only affected through a possible static-shift.

To identify changes in conductivity structure across the study area pseudosections of the apparent resistivity and phase calculated from $\boldsymbol{Z_{det}}$ have been plotted for 4 different transects as marked in Figure 1. Transect AA' runs approximately NE to SW and includes 4 sites on the schist terrain, one just to the south-west of the DMOB, and 4 sites lying in the Moonlight Tectonic Zone. Transect BB' is to the south-east of this and includes sites which lie in/on all of the major geological regions – the schist, the DMOB, the Murihiku Terrane and the Median Batholith/Brook Street Terrane. The two transects CC' and DD', further to the east both have 5 sites on the schist, one on the DMOB, and two to the south on the Murihiku Terrane.

Figure 3 shows the determinant apparent resistivity and phase pseudosections for all four transects. For transect AA' the phase pseudosection shows low phases (blue to purple) persisting to longer period (lower frequency) beneath the Murihiku Terrane (MuT) and the MTZ compared to sites on the schist. The main feature in the determinant apparent resistivity pseudosection is the large contrast between sites in the MTZ and those to the north. Although the smooth variation in phase with location suggests that the higher ρ_a values at some sites, especially 134 and 161, may be due to static-shift, it is clear that the MTZ is marked by much lower apparent resistivities. Commensurate with this, due to the much smaller skin-depth in a higher conductivity, it is likely that structure seen beneath this zone is at a much shallower depth than at sites on adjacent more resistive terrain. There is also a rise in phase values at the shortest periods beneath site 153.

The pseudosections for transect BB' show similar features across the schist and the DMOB, with the same extension of low phase to longer periods at the more south-western sites. Most noticeable is the very low ρ_a values at site 159. This site lies on the Cenozoic sediments which cover the Murihiku Terrane and the apparent resistivity shows a very large contrast with values at the adjacent site 167 which lies on the Brook Street Terrane

immediately to the east of the inferred location of the MTZ. It is possible that this reflects a connection between the MTZ and this portion of the Murihiku.

Pseudosections for transects CC' and DD' are also shown in Figure 3 and are remarkably similar. At the shortest periods there is a similar decrease in phase from north-east to south-west as seen on transects AA' and BB'. However, there is also a very noticeable change in phase at longer periods across the Dun Mountain Ophiolite Belt with markedly lower values in the south-west compared to the north-east. On both transects the single site within the DMOB also shows slightly higher $\boldsymbol{\rho_a}$ values which, given the observed change in phase, are likely not an effect of static-shift. Although there are relatively large gaps between these sites (140 and 138) and adjacent sites to the north (131 and 130), the determinant apparent resistivity and phase suggest that there is actually a band of high resistivity to the north of the DMOB.

These features can also be clearly seen in Figure 4 which shows contour plots of log10 apparent resistivity and phase across the study area at 3 different periods of variation. In particular the lower apparent resistivity associated with the MTZ, extending east into Murihiku Terrane, is very clearly evident at all three periods. Also evident at periods of 31.6 and 316 seconds is the lower phase beneath the Murihiku compared to the schist which is seen on all 4 transects in Figure 3. At the two longer periods phases higher then 45° are also seen right across the schist terrane. Higher resistivity immediately to the north of the Dun Mountain Ophiolite Belt is less obvious but can also be seen.

In summary, analysis of the determinant pseudosections, supported by individual apparent resistivity curves calculated from the impedance tensors, suggests the following:

(1) The conductivity structure in the western part of the study area where the DMOB trends S-N and is adjacent to the MTZ, and to the south of this where the Murihiku abuts the Median Batholith, is complex and clearly 3-dimensional.

(2) In this region, the MTZ marks an area of significantly lower resistivity, certainly in the near-surface but possibly to considerable depth. This is in contrast to the adjacent higher resistivity Median Batholith to the west.

(3) There are indications that parts of the Murihiku Terrane to the east of the MTZ may also have lower resistivity than areas to the north and south.

(4) Across the schist of Central Otago the structure appears relatively uniform. Phase values greater than 45° at periods longer than a few hundred seconds suggesting an increase in conductivity at depth.

(5) In the south-eastern part of the study area there is evidence for a change in conductivity structure across the DMOB. The DMOB itself, and possibly the schist immediately to the north may exhibit higher resistivity than occurs either further to the north or on the Murihiku Terrane to the south.

5. Structural implications for GIC

Although a more complete image of the conductivity structure in the region will ultimately be provided by 3-dimensional inversion modelling of the MT data, this process is non-unique. A useful and robust alternative is to simply use the measured impedances to understand what aspects of the tectonic/geological structure may have significant influence on GIC induced in this part of New Zealand. Mukhtar (2021) investigated modelling of GIC in the southern part of the South Island by using an equivalent circuit, as suggested by Boteler et al. (2013), to represent the part of the South Island transmission network north of Roxburgh (ROX) in central Otago. He found that this use of an equivalent circuit gave very little difference in calculated GIC results in the southern South Island, when compared to the GIC calculation results using the entire South Island network. The implication of this is that GIC in the southern part of the South Island are largely the result of electric fields induced within the study area and little current actually passes through Roxburgh from north to south, or vice-versa. In investigating the influence of structural elements on GIC we therefore treat the transmission network south of ROX substation as an isolated network, following the findings of Mukhtar (2021).

Actual measurements of GIC on transformers in Southland and Otago (Mac Manus et al., 2017, 2020; Divett et al. 2020) have shown that during significant geomagnetic activity very large GIC are observed in the lower South Island at substations in Dunedin, with smaller currents observed at Roxburgh, Invercargill, and Manapouri (the later being to the west of Te Anau in Fiordland, Figure 1). For example, GIC during the St. Patrick's Day geomagnetic storm of 2015 in individual transformers at substations in Dunedin (Halfway Bush – HWB and South Dunedin – SDN), Roxburgh (ROX), Invercargill (INV) and Manapouri (MAN) show peak values during the Sudden Storm Commencement of about 45 A at HWB and SDN, approximately 10 A at INV and MAN, and about 15 A at ROX. GIC's at the latter three locations were opposite in direction to those observed in Dunedin. The relative magnitudes and directions of GIC in the 5 transformers at these locations are essentially constant both over the duration of the 24 hours of the St. Patrick's Day storm and during other geomagnetic activity. Although these quoted values are for individual transformers, the numbers of grounded transformers at different substations means that the total GIC across the lower South Island do in fact sum to near zero, supporting the assertion of little current actually passing through ROX.

5.1. Induced electric fields

To investigate any possible influence of the geological and tectonic structure on the production of GIC in this part of the transmission network, it is assumed that magnetic field variations are the same across the entire study area. The validity of uing a spatially uniform magnetic field variation was tested by Divett et al. (2020), who found that it gave only minor differences in calculated geoelectric fields when compared to a spatially varying field. Any magnitude and orientation of magnetic field variation at some period can be applied to equations (1) and (2) and used to calculate the magnitude and orientation of the resulting induced electric field at an MT site. These induced electric fields, when integrated over the topology of the transmission network, result in the production of GIC.

As a starting point to understand the level of influence of geological structure on the production of GIC in this region, in Figure 5 we show the amplitude and orientations of electric fields produced in Southland/Otago by 100 nT magnetic field variations in north, east, north-west and north-east orientations for a period of 30 seconds – representative of the shortest period of variation for which data are available. The upper parts of Figure 5 show the magnitudes of the induced electric fields and there are two main features which are evident, and which reflect the contour plots of apparent resistivity shown in Figure 4. For all orientations of inducing field the low resistivity found in the Moonlight Tectonic Zone and across the western part of the Murihiku Terrane (Figure 4) results in much smaller magnitude electric fields than elsewhere in the study area. Especially for eastward and north-westward orientations of the inducing field, but also apparent for a northward inducing field, there is a relatively broad zone immediately to the north of the DMOB where the induced electric fields are significantly higher. This coincides with sites (e.g. 134, 135, 138 and 140) where the determinant apparent resistivity (Figure 3) is higher than either to the north or the south. Although, for north, north-east and north-west inducing fields, significantly higher electric fields are found to be induced at a single site close to the north-west end of the DMOB, these are likely to be the result of static-shift of the apparent resistivity as suggested by the much higher apparent resistivity at this site which is seen in Figure 4 but is not associated with any anomalous phase. Apart from these two broad features, higher induced electric fields also occur both immediately inland from Dunedin, and to the north and north-west of Invercargill, the latter corresponding to the exposed portion of the Brook Street Terrane. Significantly larger induced fields also occur on, at least, the eastern edge of the Median Batholith where it borders the Moonlight Tectonic Zone.

For each orientation of inducing magnetic field, the lower parts of Figure 5 show that, although there is some degree of scatter and a few anomalous sites, the orientations of the principal axes of the electric field ellipses is, in each case, roughly perpendicular to the orientation of the inducing field. Thus, a northward inducing field produces electric field axes which are broadly aligned east-west. It can also be noted that for north and north-east inducing fields there is a degree of agreement in the orientation of electric field axes with the orientation of the transmission lines connecting the Dunedin substations (HWB and SDN, collectively referred to as DUN) with both ROX and INV. To a large degree these transmission lines also cross the regions where the induced electric fields are larger, particularly the band of higher electric field magnitudes to the north of the DMOB. For a north-west inducing field the electric field principal axes are also broadly parallel to the transmission line from HWB/SDN to INV and are also approximately parallel to that connecting INV to ROX, although closer to INV the latter crosses the region of reduced electric field magnitude associated with the MTZ and the Murihiku Terrane. It is only for a north-east inducing field that electric field axes align with the transmission line from INV to MAN, and for the majority of its length this passes through the region of significantly smaller induced electric fields.

Although the smaller rate of change of magnetic field associated with longer period variations results in smaller magnitude induced electric fields, the patterns of induced fields shown in Figure 5 for a variation of period 30 seconds, are similar to those found for other

periods of variation. This is consistent with what is seen in Figure 4 which shows the similarity between determinant apparent resistivity and phase plots across two decades of period.

5.2. A simplified electrical model

To better assess the impact that the tectonic and geological structure, especially that associated with the MTZ/Murihiku Terrane and the DMOB, have on GIC we use a simplified calculation of currents in the network connecting the MAN, INV, ROX and Dunedin substations. Although there are multiple lines connecting some of these substations, for simplicity each connection is represented as a single line, with lengths and orientations which are approximated as listed in Table 1. With this simplification the network can broadly be represented by the circuit shown in Figure 5. In this circuit each substation is shown as earthed with a resistance R_s which represents the sum of the transformer resistance and the actual grounding resistance. Each line between substations is shown as having a resistance

Line	Length (km)	Orientation
INV - MAN	130	N42°W
DUN - INV	172	N110°W
DUN - ROX	99	N65°W
ROX - INV	124	N145°W

Table 1: Lengths and orientations of transmission lines as represented in Figure 6.

and a voltage source. Thus, R_{I-M} is the line resistance between INV and MAN, and V_{I-M} is a voltage source representing the potential difference produced between the two substations – i.e. the line integral of the electric field along the transmission line. Following Divett et al. (2017) we take R_s as 1.1 Ω and the line resistances as 0.05 Ω/km. If the currents (GIC) at each substation and in each line are represented as shown, as detailed in the Appendix, Kirchhoff's Laws can be applied to calculate the resulting currents from the matrix equation

$$\begin{pmatrix} -1 & 0 & 0 & 0 & 1 & 0 & 0 & 0 \\ 0 & -1 & 0 & 0 & -1 & 1 & 0 & 0 \\ 0 & 0 & -1 & 0 & 0 & -1 & -1 & 0 \\ 0 & 0 & 0 & -1 & 0 & 0 & 1 & -1 \\ -R_s & R_s & 0 & 0 & -R_{I-M} & 0 & 0 & 0 \\ 0 & -R_s & R_s & 0 & 0 & -R_{D-I} & 0 & 0 \\ 0 & 0 & R_s & -R_s & 0 & 0 & -R_{D-R} & 0 \\ 0 & -R_s & 0 & R_s & 0 & 0 & 0 & -R_{R-I} \end{pmatrix} \begin{pmatrix} I_M \\ I_I \\ I_D \\ I_R \\ I_{I-M} \\ I_{D-I} \\ I_{D-R} \\ I_{R-I} \end{pmatrix} = \begin{pmatrix} 0 \\ 0 \\ 0 \\ 0 \\ -V_{I-M} \\ -V_{D-I} \\ -V_{D-R} \\ -V_{R-I} \end{pmatrix}$$

The values for the voltages for a particular orientation of inducing magnetic field may be estimated by taking a map of the induced fields showing the simplified transmission lines, and superimposing on it a grid of 0.5 degrees in latitude and longitude (e.g. for a northward inducing field as shown in Figure 7(a)). For those grid cells through which a transmission line passes (A to K in Figure 7(b)), for each orientation of the inducing magnetic field the magnitude of the induced electric field and its orientation are calculated as the average of the

values at each of the MT sites in that grid cell. Table 2 shows the result of this process for a northward oriented inducing magnetic field. As can be seen, induced electric field orientations cluster around N90-110°W, and reflecting their location straddling the MTZ and the western portion of the Murihiku, cells B, G and H have by far the lowest average electric field magnitudes. Comparable values for north-east and north-west oriented inducing fields are given in the Appendix.

The potential difference between the ends of each transmission line is now calculated as

$$V = \sum \underline{E} \,.\, \underline{dl} \qquad (4)$$

where $\underline{dl}$ represents the length of transmission line in a particular grid cell, and $\underline{E}$ the vector electric field in that cell. The scalar product resolves the field in the cell onto the orientation of the transmission line. Summation over all the grid cells that the transmission line passes through then gives the potential difference.

The influence of specific tectonic/geological features on GIC can be assessed by omitting particular structural features as shown on the maps in Figure 4. Specifically, the effect of the MTZ and Murihiku on the production of GIC can be tested by replacing the low electric field regions in cells B, G and H associated with the MTZ/Murihiku Terrane with fields of 1000 mV/km, a value which represents the approximate average of the electric field magnitude at all the MT sites, and is found to be independent of the orientation of the inducing field. Given the relatively large size of the grid cells the manner in which to test the impact of the higher electric fields to the north of the DMOB is less clear. Given this limitation this has been attempted by replacing the broad band of higher (≥ 1000 mV/km) electric fields north of the DMOB (cells C, D, E, F, J and K) by fields of 800 mV/km. This, by necessity, includes a significant portion of the south-western part of the schist terrane, and, indeed, means that for a north-east inducing field the assumed electric field in cell D is actually increased (see Appendix). As a result of these limitations any clear effect of removing the DMOB is probably minimized. In any event, although calculations using such a simplified model are necessarily an approximation, the results of such an anlysis do prove useful in investigating the manner in which these structural features effect the magnitudes of GIC at the four substations.

Cell	Estimated E field (mV/km)	Average electric field orientation		Cell	Estimated E field (mV/km)	Average electric field orientation
A	4417	N103°W		G	301	N100°W
B	319	N90°W		H	120	N69°W
C	1057	N111°W		I	718	N90°W
D	950	N111°W		J	965	N69°W
E	1231	N108°W		K	1589	N80°W
F	1519	N111°W				

Table 2: Average values of the magnitude and orientation of induced electric fields in each grid cell for a northward inducing field of magnitude 100 nT at period 30 s.

5 .3.

Results

The results of calculations for north, north-east and north-west oriented 100 nT inducing magnetic fields, based on the magnitudes of induced electric fields calculated for a period of 30 s, are shown graphically in Figure 8.

The calculation of currents for the full structure (green bars in Figure 8), show that GIC at DUN are opposite in sign to GIC at MAN for all orientations of the inducing magnetic field (Figures 8(a), (c) and (e)). This is unsurprising given that DUN and MAN can be regarded as being at the eastern and western ends of the transmission line network respectively. It can also be seen that the sense of GIC at both INV and ROX depends on the orientation of the inducing field, reflecting the fact that these two substations can be regarded as intermediate between DUN and MAN, with the sense of GIC heavily dependent on the distribution of currents in the transmission lines.

As noted above, large GIC are commonly seen at the DUN substations. The overall pattern of calculated GIC seen in Figure 8 suggests that the origin of these large GIC differs depending on the orientation of the inducing magnetic field. For a northward inducing field the large GIC at DUN are associated with oppositely oriented GIC at both INV and MAN, with only very small GIC at ROX. However, for a north-east oriented inducing field the large negative GIC at DUN are related to significant positive GIC at ROX and MAN, with only very small GIC at INV. With a north-west inducing field orientation GIC at ROX are of the same sense as at DUN and are balanced by opposite GIC at both INV and MAN.

Removal of the low electric fields seen in the MTZ and Murihiku Terrane (red bars in Figure 8) leads to a significant increase in current in the transmission line between INV and MAN for both north and north-east oriented inducing fields (Figures 8(b) and 8(d)). In both cases this leads to an increase in GIC at MAN of near 100% (Figures 8(a) and 8(c)). For a northward inducing field removal of the MTZ leads to a decrease in GIC at INV of ~5 A (Figure 8(a)). As, for this inducing field, GIC at INV have the same sense as GIC at MAN this implies that the increase in GIC at MAN, and the increased INV-MAN current, come not solely from the reduced GIC at INV but are also due to the increase in currents in both the DUN-INV and ROX-INV transmission lines (Figure 8(b)). In contrast, for a north-eastward inducing field GIC at INV have the opposite sign to those at MAN. Thus, the very large increase in current in the INV-MAN line (Figure 8(d)) can be seen to be primarily a result of current flowing into the line at INV and out at MAN. For a northward inducing field GIC at ROX are very small and appear independent of the MTZ structure. While GIC at ROX are larger for a north-east inducing field (Figure 8(c)) they are similarly essentially independent of the presence of absence of the low electric fields in the MTZ/Murihiku. For a north-west inducing field (Figures 8(e) and (f)) the fact that the INV-MAN transmission line is near parallel to this orientation means that, although there is some redistribution of both GIC and currents in the transmission lines, including a reversal of GIC at ROX, the overall effect of removing the MTZ is very small.

Although it appears that the presence of the region of low resistivity and small induced electric fields associated with the MTZ are responsible for the relatively small GIC seen at MAN, the impact of the DMOB is much less clear. As indicated this probably partly

reflects the difficulty in representing the region of enhanced electric fields on the chosen 0.5° scale, but, nonetheless, some inferences can be drawn from Figure 8. In particular it can be seen (Figures 8(a) and (e)) that, for inducing fields oriented north and north-west, removing the high electric field values associated with cells C, D, E, F, J and K leads to a reduction in the size of GIC at both DUN and INV. This is entirely consistent with an associated reduction in current in the DUN-INV transmission line seen in Figures 8(b) and (f). At DUN the drop in GIC is between 4 and 6 A, for both orientations of inducing field about 20% of the value calculated with the full structure, whilst at INV the reductions in GIC are closer to 25%. At ROX GIC are negative (i.e into the substation, Figure 6) for both these orientations of inducing field. There is very little change in currents for a north-east oriented inducing field. Again, this probably reflects the relationship between the orientation of the inducing field and the transmission lines. The north-east inducing field orientation is very close to that of the ROX-INV transmission line and leads to only a very small potential difference between ROX and INV, while there is a much reduced potential difference between DUN and INV compared to the other two orientations of inducing field.

6. Conclusion

In summary, although the limitations of such a simplified calculation must be emphasised, the results suggest that the tectonic/geological structure in southern South Island, and the way it has resulted in electrical conductivity variations, does have a impact on GIC. Most obvious and significant is that smaller induced electric fields, associated with the higher conductivity of the Moonlight Tectonic Zone and the Murihiku Terrane, clearly have the effect of reducing the GIC observed at MAN. Without this zone of significantly reduced electric fields any inducing field with a predominantly north to north-east orientation (which encompasses local magnetic north) would result in much larger GIC at MAN. The resultant increased current between INV and MAN would also have an impact on other substations.

For north and north-west oriented inducing magnetic field, the higher induced electric fields associated with DMOB, and to its north, appears to be a contributor to the large GIC which are observed at the Dunedin substations. Although the calculated effect of removing the DMOB as described is gives a reduction of ~5 A at DUN, the very broad manner in which the DMOB has been represented in this calculation likely means that its true contribution to the large GIC at DUN is greater. Adjustments to the transmission line model (Figure 6) such as including bends in the lines are also likely to have only a secondary effect on the calculated currents. This is consistent Divett et al. (2020) who found that assumption of linearity of transmission lines made little difference in the actual calculation of GIC.

Both the magnitude and sense of GIC at both INV and ROX are highly dependent on the orientation of the inducing field. At INV the orientation of induced electric field relative to the transmission lines from the other three substations is important in determining the significance of both the MTZ and the DMOB. At ROX neither has much impact on GIC.

GIC produced in a power network result from the integral of the electric field, induced by magnetic activity, along the length of the powerlines. The magnitude of induced electric fields is dependent not only on the rate of change of the magnetic field, but also on

the electrical conductivity of the ground. The orientation of the induced fields is similarly dependent not only on the orientation of the inducing magnetic field, but on the spatial distribution of conductivity. Thus, in any region that is susceptible to the generation of GIC in transmission lines, a knowledge of the spatial distribution of magnitudes and orientations of the induced electric field is important for understanding GIC. This work thus emphasises the importance of improved ground conductivity measurements in GIC-focused Space Weather studies. It also helps explain the very high GIC regularly reported in Dunedin, and why the transformers in that city has been identified as particularly high risk during an extreme space weather event (Mac Manus et al., 2022b).

Acknowledgments

This research, including scholarship funding for KP, was supported by the New Zealand Ministry of Business, Innovation and Employment Endeavour Fund Research Programme contract UOOX2002. We thank two anonymous reviewers for suggestions which have helped to improve this paper.

Data Availability Statement

The magnetotelluric data in the form of edi files may be accessed at https://doi.org/10.6084/m9.figshare.21944564.v1.

References

Bailey, R.L., T.S. Halbedl, I. Schattauer, A. Römer, G. Achleitner, C.D. Beggan, V. Wesztergom, R. Egli, & R. Leonhardt (2017). Modelling geomagnetically induced currents in midlatitude Central Europe using a thin-sheet approach. *Annales Geophysicae*, 35, 751–761, doi:10.5194/angeo-35-751-2017.

Bailey, R. L., T.S. Halbedl, I. Schattauer, G. Achleitner & R. Leonhardt (2018). Validating GIC models with measurements in Austria: Evaluation of accuracy and sensitivity to input parameters. *Space Weather*,16, 887–902, doi:10.1029/2018SW001842.

Ballance, P. (2009). New Zealand geology: an illustrated guide. Geological Society of New Zealand Miscellaneous Publication No. 148, 397 pp.

Bedrosian, P. A., & J. J. Love (2015). Mapping geoelectric fields during magnetic storms: Synthetic analysis of empirical United States impedances. *Geophysical Research Letters,* 42, 10,160–10,170, doi:10.1002/2015GL066636.

Beggan, C.D., D. Beamish, A. Richards, G.S. Kelly, G.S. & A.W. Thomson (2013). Prediction of extreme geomagnetically induced currents in the UK high-voltage network. *Space Weather*, 11, 407-419, doi:10.1002/swe.20065.

Bibby, H.M., T.G. Caldwell & C. Brown (2005). Determinable and non-determinable parameters of galvanic distortion in magnetotellurics. *Geophysical Journal International,* 163, 915–930, doi: 10.1111/j.1365-246X.2005.02779.x

Blake, S.P., P.T. Gallagher, J. McCauley, A.G. Jones, C. Hogg, J. Campanya, C. Beggan, A.W.P. Thomson, G.S. Kelly & D. Bell (2016). Geomagnetically induced currents in the

517 Irish power network during geomagnetic storms. *Space Weather*, 14, 1136–1154,
518 doi:10.1002/2016SW001534.

519 Boteler D.H., A.J.C. Lackey, L. Marti & S. Shelemy (2013). Equivalent circuits for
520 modelling geomagnetically induced currents from a neighbouring network. *IEEE Power &*
521 *Energy Society General Meeting*, Vancouver, BC, 2013, pp. 1-5,
522 doi:10.1109/PESMG.2013.6672982.

523 Caldwell, T.G., H.M. Bibby & C. Brown (2004). The magnetotelluric phase tensor.
524 *Geophysical Journal International,* 158**,** 457–469, doi:10.1111/j.1365-246X.2004.02281.x

525 Campanyà, J., P.T. Gallagher, S.P. Blake, M. Gibbs, D. Jackson, C.D. Beggan, G.S.
526 Richardson, & C. Hogg (2019). Modeling geoelectric fields in Ireland and the UK for space
527 weather applications. *Space Weather*, 17, 216–237, doi:10.1029/2018SW001999.

528 Dimmock, A.P., L. Rosenqvist, D.T. Welling, A. Viljanen, I. Honkonen, R.J. Boynton & E.
529 Yordanova (2020). On the regional variability of dB/dt and its significance to GIC. *Space*
530 *Weather*, 18, e2020SW002497, doi: 10.1002/2020SW002497.

531 Divett, T., M. Ingham, C.D. Beggan, G.S. Richardson, C.J. Rodger, A.W.P. Thomson & M.
532 Dalzell (2017). Modeling geo-electric fields and geomagnetically induced currents (GIC)
533 around New Zealand to explore GIC in the South Islands's electrical transmission network.
534 *Space Weather*, 15, 1396-1412, doi:10.1002/2017SW001697.

535 Divett, T., G.S. Richardson, C.D. Beggan, C.J. Rodger, D.H. Boteler, M. Ingham, D.H. Mac
536 Manus, A.W.P. Thomson & M. Dalzell (2018). Transformer-level modeling of
537 geomagnetically induced currents in New Zealand's South Island. *Space Weather*, 16, 718-
538 735, doi:10.1029/2018SW001814.

539 Divett, T., D.H. Mac Manus, G.S. Richardson, C.D. Beggan, C.J. Rodger, M. Ingham, E.
540 Clarke, A.W.P. Thomson, M. Dalzell & Y. Obana (2020). Geomagnetically induced current
541 model validation from New Zealand's South Island. *Space Weather*, 18, doi:
542 10.1029/2020SW002494.

543 Hunt, T. (1978). Stokes magnetic anomaly system. *New Zealand Journal of Geology and*
544 *Geophysics*, 21, 595-606, doi:10.1080/00288306.1978.10424087.

545 Ingham, M. (1988). The use of invariant impedances in magnetotelluric interpretation.
546 *Geophysical Journal*, 92, 165-169, doi:10.1111/j.1365-246X.1988.tb01130.x

547 Ingham, M. (1996). Magnetotelluric soundings across the South Island of New Zealand:
548 Electrical structure associated with the orogen of the Southern Alps. *Geophysical Journal*
549 *International*, 124(1), 134–148, doi:10.1111/j.1365-246x.1996.tb06358.x

550 Ingham, M., C.J. Rodger, T. Divett, M. Dalzell & T. Petersen (2017). Assessment of GIC
551 based on transfer function analysis. *Space Weather*, 15, 1615-1627,
552 doi:10.1002/2017SW001707.

553 Kelbert, A. & G.M. Lucas (2020). Modified GIC estimation using 3-D earth conductivity.
554 *Space Weather*, 18, e2020SW002467, doi:10.1029/2020SW002467.

555 King R.P. (2000) Tectonic reconstructions of New Zealand: 40 Ma to the Present. *New*
556 *Zealand Journal of Geology and Geophysics*, 43, 611-638,
557 doi:10.1080/00288306.2000.9514913.

558 Love, J. J., G.M. Lucas, A. Kelbert & P.A. Bedrosian (2018a). Geoelectric hazard maps for
559 the Mid-Atlantic United States: 100 year extreme values and the 1989 magnetic storm.
560 *Geophysical Research Letters*, 45, 5–14, doi: 10.1002/2017GL076042.

561 Love, J. J., G.M. Lucas, P.A. Bedrosian & A. Kelbert (2018b). Extreme-value geoelectric
562 amplitude and polarization across the northeast United States. *Space Weather*, 17, 379-395,
563 doi: 10.1029/2018SW002068.

564 Mac Manus, D. H., C.J. Rodger, M. Dalzell, A.W.P. Thomson, M.A. Clilverd, T. Petersen,
565 M.M. Wolf, N.R. Thomson & T. Divett (2017). Long term geomagnetically induced current
566 observations in New Zealand: Earth return corrections and geomagnetic field driver. *Space*
567 *Weather*, 15, 1020–1038, doi:10.1029/2017SW001635

568 Mac Manus, D.H., C.J. Rodger, M. Ingham, M.A. Clilverd, M. Dalzell, T. Divett, G.S.
569 Richardson, & T. Petersen (2022a). Geomagnetically induced current model in New Zealand
570 across multiple disturbances: validation and extension to non-monitored transformers. *Space*
571 *Weather*, 20, e2021SW002955, doi: 10.1029/2021SW002955.

572 Mac Manus, D.H., C.J. Rodger, M. Dalzell, A. Renton, G.S. Richardson, T. Petersen & M.A.
573 Clilverd (2022b). Geomagnetically induced current modeling in New Zealand: extreme storm
574 analysis using multiple disturbance scenarios and industry provided hazard magnitudes.
575 *Space Weather*, 20, e2022SW003320, doi: 10.1029/2022SW003320.

576 Marshalko, E., M. Kruglyakov, A. Kushinov, B.S. Murphy, L. Rastatter, C. Ngwira, & A.
577 Pulkkinen (2020).Exploring the influence of lateral conductivity contrasts on the storm time
578 behavior of the ground electric field in the eastern United States. *Space Weather*, 18,
579 e2019SW002216, doi:10.1029/2019/2019SW002216.

580 Marti, A., P. Queralt, J. Ledo (2009). WALDIM: A code for the dimensionality analysis of
581 magnetotelluric data using the rotational invariants of the magnetotelluric tensor. *Computers*
582 *& Geosciences,* 35, 2295-2303*,* doi:10.1016/j.cageo.2009.03.004.

583 McKay, A. J. & K. A. Whaler (2006). The electric field in northern England and southern
584 Scotland: Implications for geomagnetically induced currents, *Geophysical Journal*
585 *International*, 167, 613–625, doi:10.1111/j.1365-246X.2006.03128.x.

586 Mortimer, N., Davey, F., Melhuish, A., Yu, J. & Godfrey, N.J. (2002). Geological
587 interpretation of a deep seismic reflection profile across the eastern Province and Medial
588 Batholith, New Zealand: crustal architecture of an extended Phanerozoic convergent margin.
589 *New Zealand Journal of Geology and Geophysics*, 45, 349-363,
590 doi:10.1080/00288306.2002.9514978

591 Mukhtar, K. (2021). Geomagnetically induced currents in the New Zealand power system.
592 Unpublished PhD Thesis, Victoria University of Wellington, pp. 285.

593 Mukhtar, K., M. Ingham, C.J. Rodger, D.H. Mac Manus, T. Divett, W. Heise, E. Bertrand, M. Dalzell,
594 M. & T. Petersen (2020). Calculation of GIC in the North Island of New Zealand using MT data and
595 thin-sheet modelling. *Space Weather*, 18, e2020SW002580, doi: 10.1029/2020SW002580

596 Myllys, M., A. Viljanen, Ø.A. Rui, & T.M. Ohnstad (2014). Geomagnetically induced
597 currents in Norway: the northernmost high-voltage power grid in the world. Journal of Space
598 Weather and Space Climate, 4, A10, doi:10.1051/swsc/2014007.

599 Nakamura, S., Y. Ebihara,, S. Fujita, T. Goto, N. Yamada, S. Watari & Y. Omura (2018).
600 Time domain simulation of geomagnetically induced current (GIC) flowing in 500-kV power
601 grid in Japan including a three-dimensional ground inhomogeneity. *Space Weather*, 16, 1946-
602 1959, doi:10.1029/2018SW002004.

603 Sutherland, R., F. Davey, F. & J. Beavan (2000). Plate boundary deformation in South Island,
604 New Zealand, is related to inherited lithospheric structure. *Earth and Planetary Science*
605 *Letters*, 177, 141–151, doi:10.1016/S0012-821X(00)00043-1.

606 Torta, J.M., A. Marcuello, J. Campanyà, S. Marsal, P. Queralt & J. Ledo (2017). Improving
607 the modeling of geomagnetically induced currents in Spain. *Space Weather*, 15, 691-703, doi:
608 10.1002/2017SW001628.

609 Viljanen, A. (1997). The relation between geomagnetic variations and their time derivatives
610 and implications for estimation of induction risks. *Geophysical Research Letters*, 24, 631-
611 634, doi:10.1029/97GL00538.

612 Viljanen, A., H. Nevanlinna, K. Pajunpää & A. Pulkkinen (2001). Time derivative of the
613 horizontal geomagnetic field as an activity indicator. *Annales Geophysicae*, 19, 1107-1118,
614 doi:10.5194/angeo-1107-2001.

615 Viljanen, A. & R. Pirjola (2017). Influence of spatial variations of the geoelectric field on
616 geomagnetically induced currents. *Journal of Space Weather and Space Climate*, 7, A22,
617 doi:10.1051/swsc/2017024.

618 Wannamaker, P. E., G.R. Jiracek, J.A. Stodt, T.G.Caldwell, V.M.Gonzalez, J.D. McKnight &
619 A.D. Porter (2002). Fluid generation and pathways beneath an active compressional orogen,
620 the New Zealand Southern Alps, inferred from magnetotelluric data. *Journal of Geophysical*
621 *Research*, 107(B6), 1–20, doi:10.1029/2001JB000186.

622 Wannamaker, P. E., T.G. Caldwell, G.R. Jiracek, V. Maris, G.J. Hill, Y. Ogawa, H.M. Bibby,
623 S.L. Bennie & W. Heise (2009). Fluid and deformation regime of an advancing subduction
624 system at Marlborough, New Zealand. *Nature*, 460(7256), 733–736,
625 doi:10.1038/nature08204.

626 Watari, S., S. Nakamura & Y. Ebihara (2021). Measurement of geomagnetically induced
627 current (GIC) around Tokyo, Japan. *Earth Planets Space*, 73**,** 102, doi:10.1186/s40623-021-
628 01422-3.

629 Weaver, J.T., A.K. Agarwal, & F.E.M. Lilley (2000). Characterisation of the magnetotelluric
630 tensor in terms of its invariants. *Geophysical Journal International*, 141, 321–336.

631 Wik, M., R. Pirjol, H. Lundstedt, A. Viljanen, P. Wintoft & A. Pulkkinen (2009). Space
632 weather events in July 1982 and October 2003 and the effects of geomagnetically induced
633 currents on Swedish technical systems. *Annales Geophysicae*, 27, 1775–1787.

634

635 **Appendix**

636 **1. Calculation of currents**

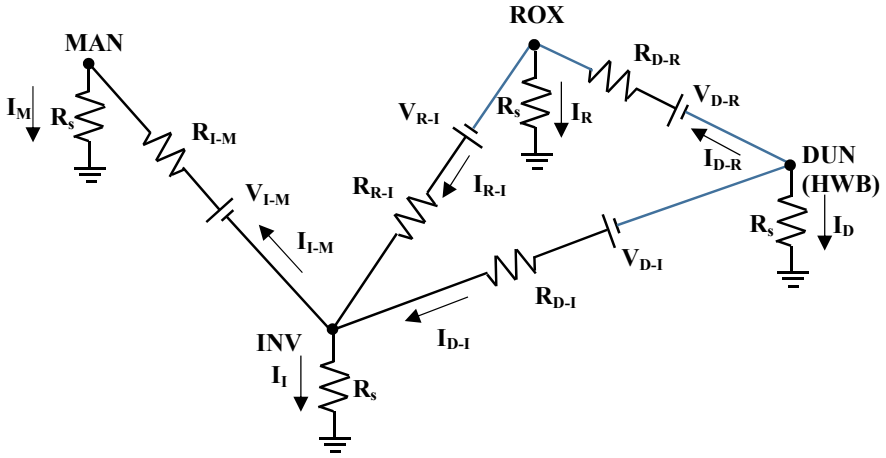

Figure A-1: Simplified circuit for assessing the impact of structure on calculated GIC.

637 Taking the circuit diagram shown in Figure A-1, applying current continuity at each
638 node leads to:

639 $$-I_M + I_{I-M} = 0 \qquad \text{(A1)}$$

640 $$-I_I - I_{I-M} + I_{D-I} = 0 \qquad \text{(A2)}$$

641 $$-I_D - I_{D-I} - I_{D-R} = 0 \qquad \text{(A3)}$$

642 $$-I_R + I_{D-R} - I_{R-I} = 0 \qquad \text{(A4)}$$

643 Applying Kirchhoff's loop law around each loop between earths gives 4 more equations:

644 $$V_{I-M} - I_{I-M}R_{I-M} - I_M R_s + I_I R_s = 0 \qquad \text{(A5)}$$

645 $$V_{D-I} - I_{D-I}R_{D-I} - I_I R_s + I_D R_s = 0 \qquad \text{(A6)}$$

646 $$V_{D-R} - I_{D-R}R_{D-R} - I_R R_s + I_D R_s = 0 \qquad \text{(A7)}$$

647 $$V_{R-I} - I_{R-I}R_{R-I} - I_I R_s + I_R R_s = 0 \qquad \text{(A8)}$$

648 These 8 equations can be rearranged into the matrix relationship:

$$\begin{pmatrix} -1 & 0 & 0 & 0 & 1 & 0 & 0 & 0 \\ 0 & -1 & 0 & 0 & -1 & 1 & 0 & 0 \\ 0 & 0 & -1 & 0 & 0 & -1 & -1 & 0 \\ 0 & 0 & 0 & -1 & 0 & 0 & 1 & -1 \\ -R_S & R_S & 0 & 0 & -R_{I-M} & 0 & 0 & 0 \\ 0 & -R_S & R_S & 0 & 0 & -R_{D-I} & 0 & 0 \\ 0 & 0 & R_S & -R_S & 0 & 0 & -R_{D-R} & 0 \\ 0 & -R_S & 0 & R_S & 0 & 0 & 0 & -R_{R-I} \end{pmatrix} \begin{pmatrix} I_M \\ I_I \\ I_D \\ I_R \\ I_{I-M} \\ I_{D-I} \\ I_{D-R} \\ I_{R-I} \end{pmatrix} = \begin{pmatrix} 0 \\ 0 \\ 0 \\ 0 \\ -V_{I-M} \\ -V_{D-I} \\ -V_{D-R} \\ -V_{R-I} \end{pmatrix} \quad \text{(A9)}$$

which, with assumed values for R_S, the resistance per km of the transmission lines, and estimated values for the voltages, may be solved for the eight currents.

2. Magnitudes and orientations of induced electric fields.

The tables below show the average values of the magnitude and orientation of the induced electric field in each grid cell (as shown in Figure 7) for north, north-east and north-west orientations of the inducing magnetic field for a period of 30 seconds.

Cell	Average E field (mV/km)	Average electric field orientation		Cell	Average E field (mV/km)	Average electric field orientation
A	4417	N103°W		G	301	N100°W
B	319	N90°W		H	120	N69°W
C	1057	N111°W		I	718	N90°W
D	950	N111°W		J	965	N69°W
E	1231	N108°W		K	1589	N80°W
F	1519	N111°W				

Table A2-1: Average values of the magnitude and orientation of induced electric fields in each grid cell for a northward inducing field of magnitude 100 nT at period 30 s.

Cell	Average E field (mV/km)	Average electric field orientation		Cell	Average E field (mV/km)	Average electric field orientation
A	4354	N101°W		G	225	N55°W
B	320	N48°W		H	146	N43°W
C	927	N44°W		I	570	N39°W
D	348	N61°W		J	967	N41°W
E	1072	N54°W		K	1451	N40°W
F	1243	N83°W				

Table A2-2: Average values of the magnitude and orientation of induced electric fields in each grid cell for a north-eastward inducing field of magnitude 100 nT at period 30 s.

Cell	Average E field (mV/km)	Average electric field orientation		Cell	Average E field (mV/km)	Average electric field orientation
A	2212	N107°W		G	265	N134°W
B	601	N104°W		H	86	N135°W
C	1340	N145°W		I	684	N122°W
D	1159	N128°W		J	672	N114°W
E	953	N124°W		K	1518	N121°W
F	1031	N113°W				

Table A2-3: Average values of the magnitude and orientation of induced electric fields in each grid cell for a north-westward inducing field of magnitude 100 nT at period 30 s.

662

663

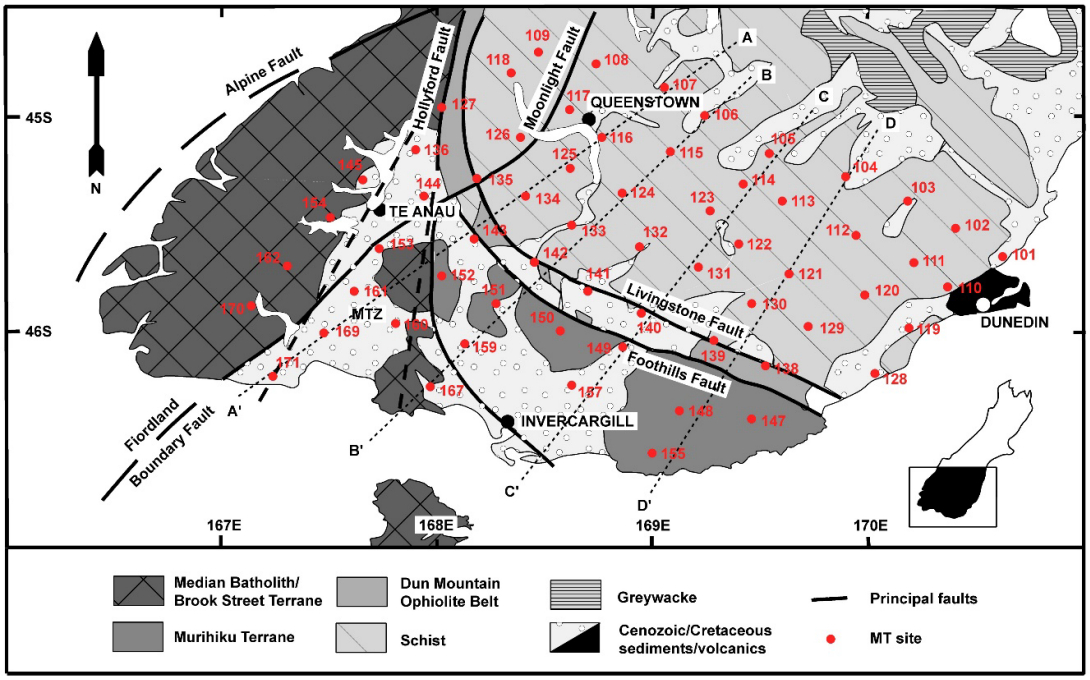

Figure 1: Generalized geology and tectonic structure of the study area and location of MT sites. Dotted lines mark the pseudosection transects shown in Figure 3.

664

665

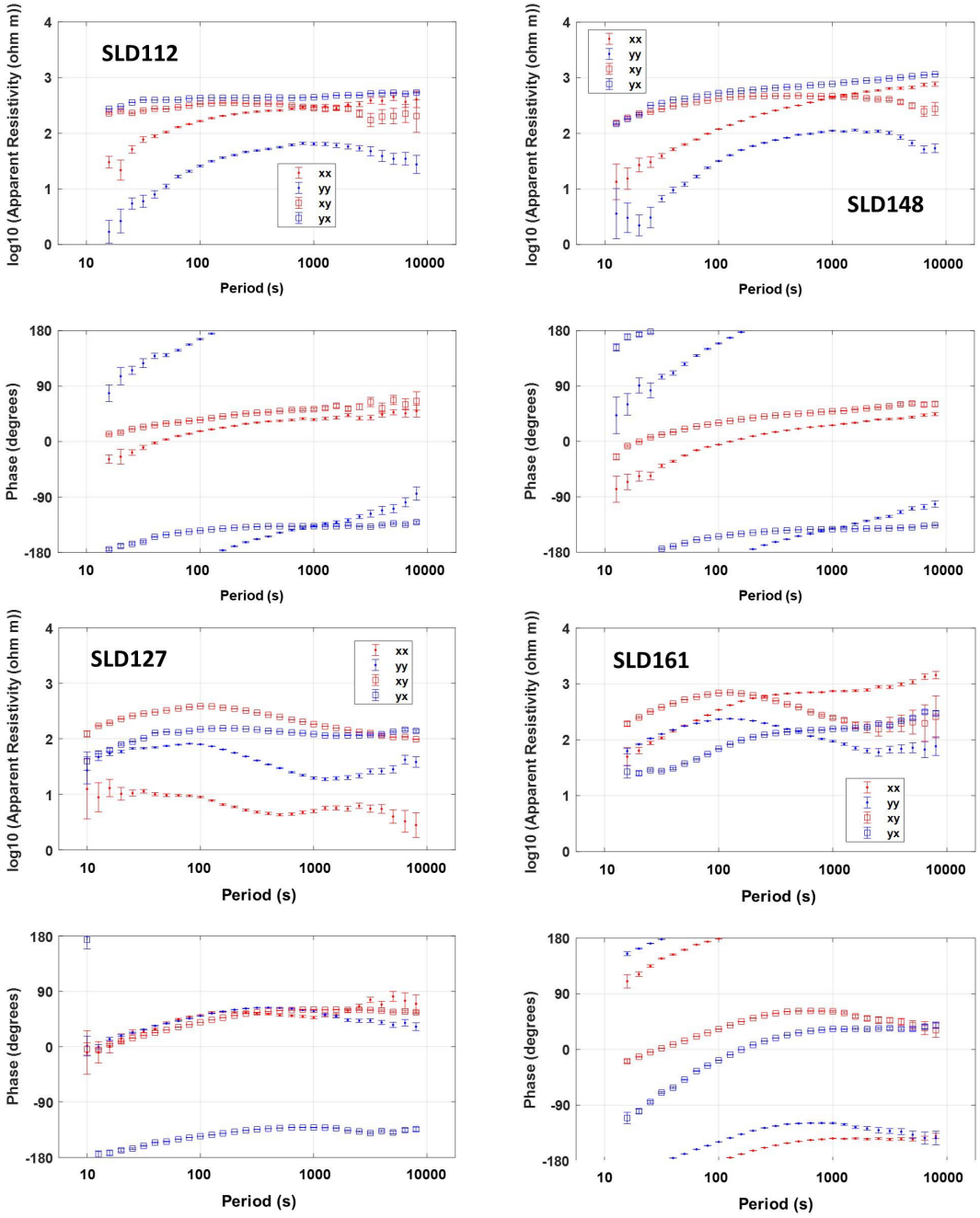

Figure 2: MT apparent resistivity and phase curves from sites SLD112 (Haast schist), SLD148 (Murihiku Terrane), SLD127 Median Batholith), and SLD161 (Moonlight Tectonic Zone).

666

667

668

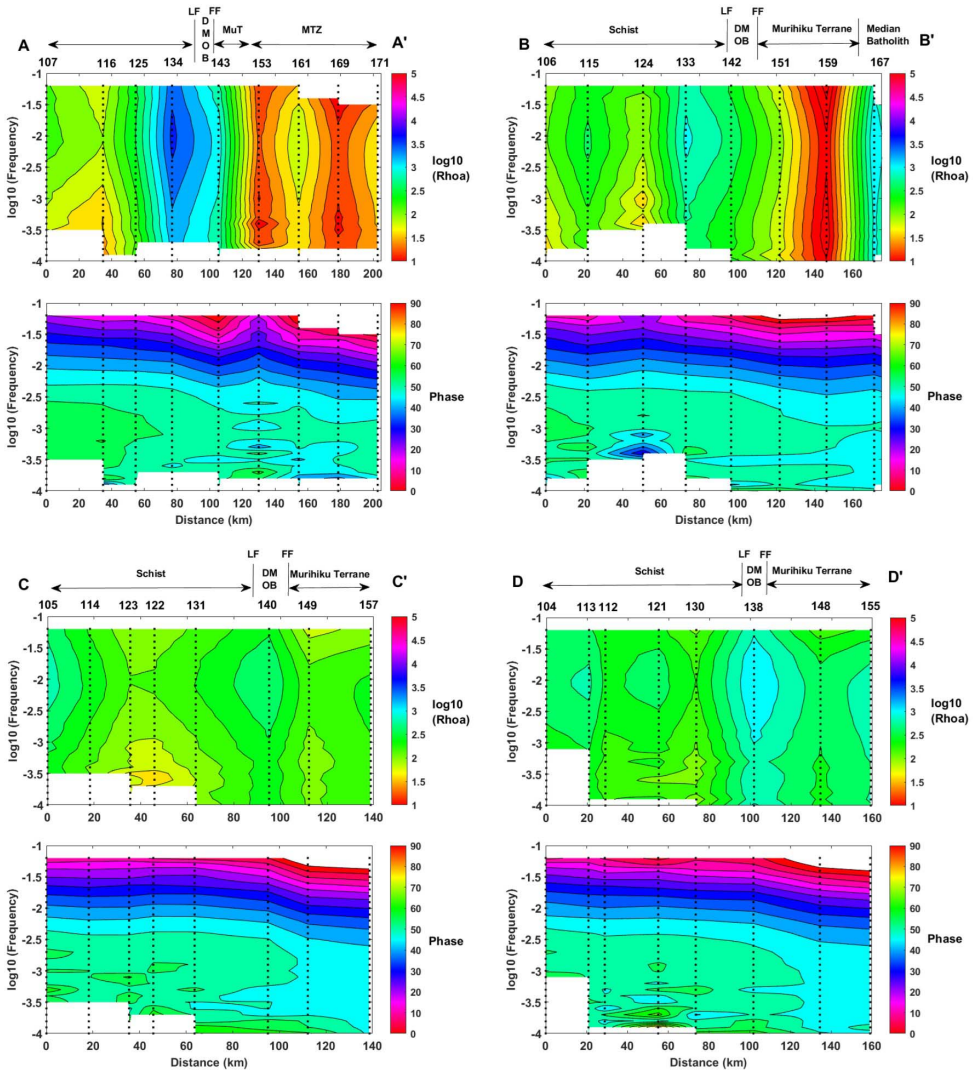

Figure 3: Pseudosections of log10 apparent resistivity (Rhoa) and phase calculated from the determinant impedance for transects AA' to DD' as marked in Figure 1.

669

670

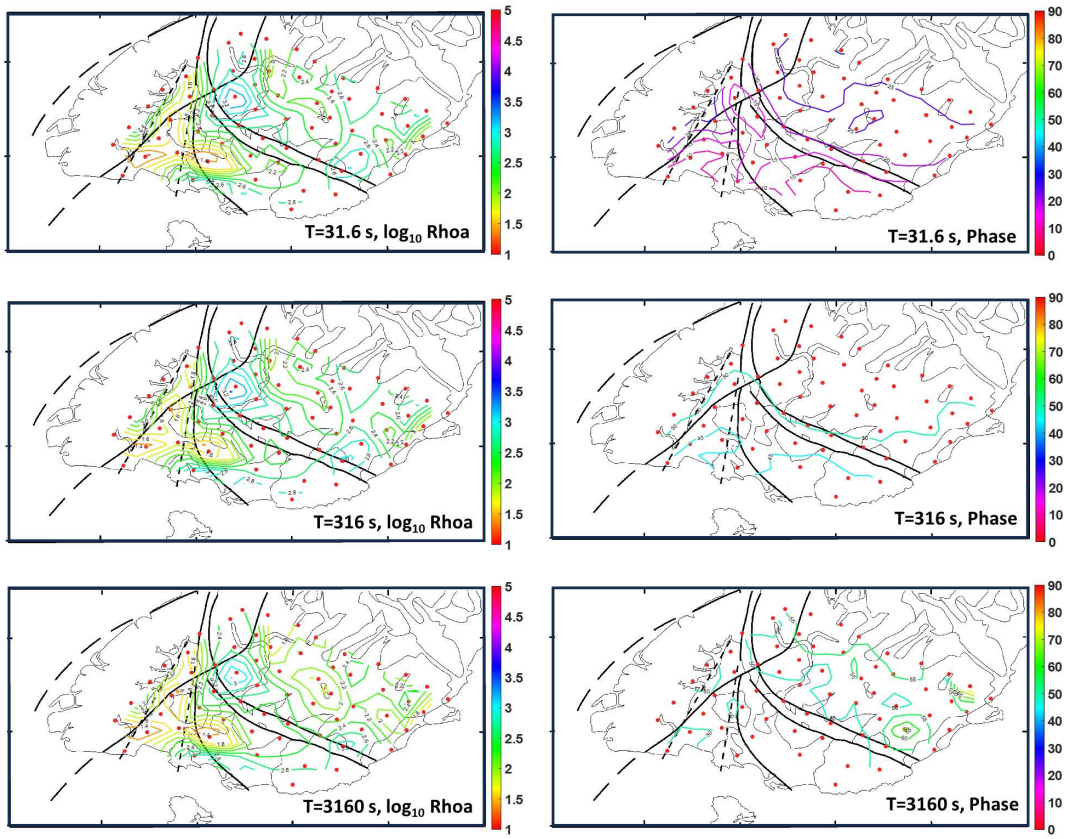

Figure 4: Contour plots of log10 apparent resistivity (Rhoa) and phase calculated from the determinant impedance for three periods of variation.

671

672

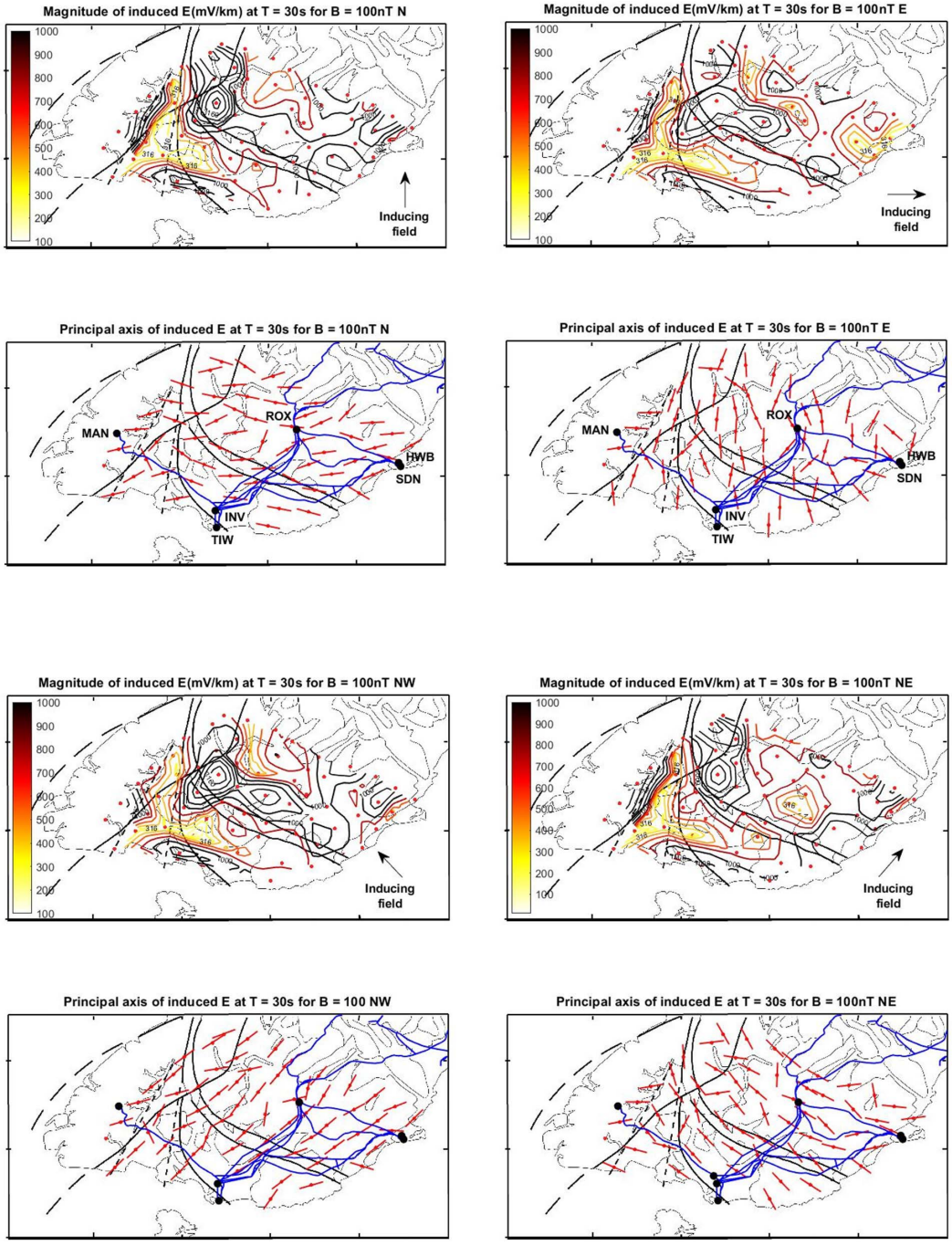

Figure 5: Magnitudes and principal axes of electric fields induced by a 100 nT variation in the magnetic field in north, east, north-west and north-east orientations. The locations of substations mentioned in the text are also shown, and the locations of high-voltage power transmission lines are shown in blue.

673

674

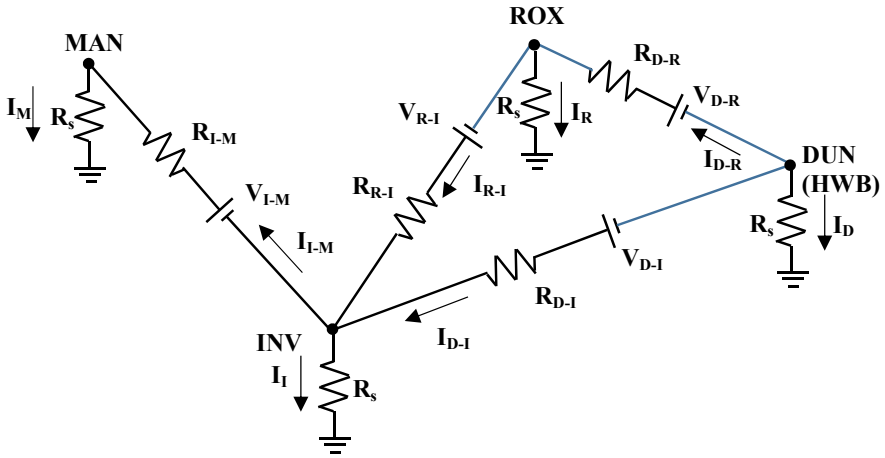

Figure 6: Simplified circuit for assessing the impact of structure on calculated GIC.

675

676

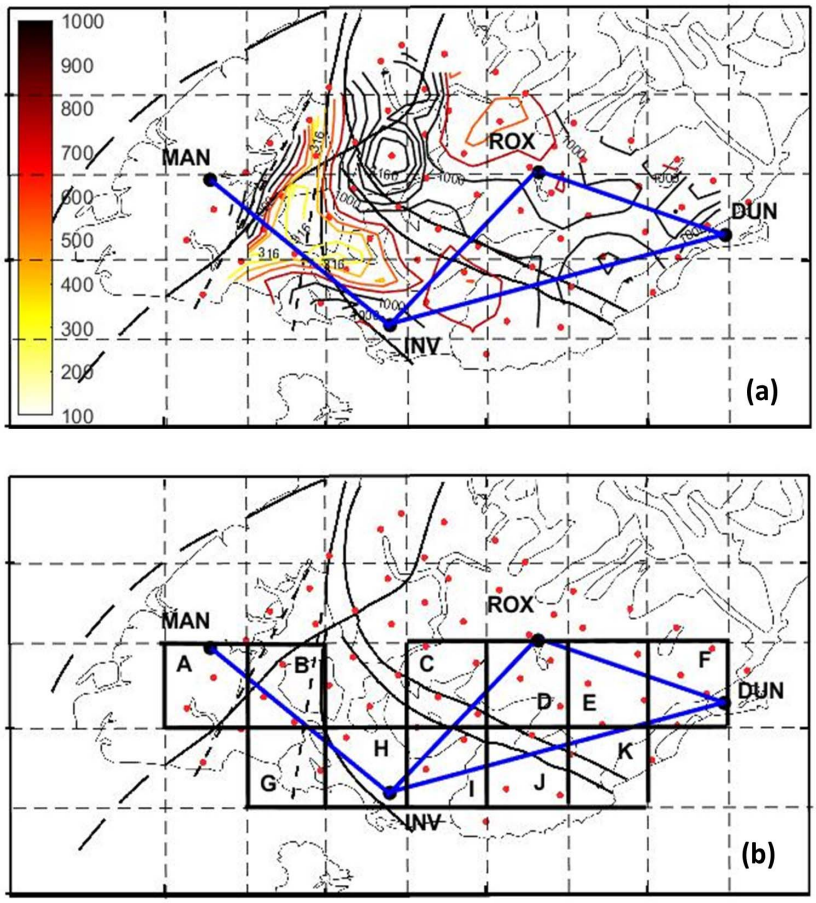

Figure 7: (a) Superimposition of a 0.5 degree grid on to a map of induced electric field magnitude; (b) identification of grid cells that the simplified transmission line network passes through.

677

678

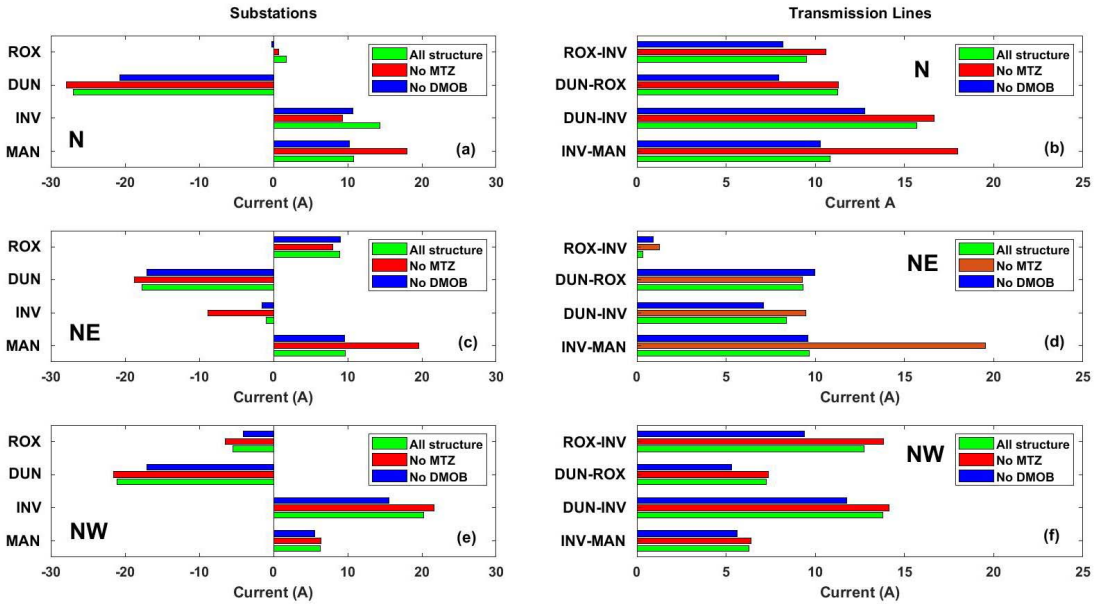

Figure 8: Calculated currents (GIC) at substations and in transmission lines for three orientations of the inducing magnetic field as indicated. Green bars – currents calculated when including the effect of all geological structures; red bars – currents calculated with the effect of the Moonlight tectonic Zone removed; blue bars – currents calculated with the effect of the Dun Mountain Ophiolite Belt removed.

679

680

681

Figure 1.

N

Alpine Fault

Hollyford Fault

Moonlight Fault

Livingstone Fault

Foothills Fault

Fiordland Boundary Fault

QUEENSTOWN

TE ANAU

MTZ

INVERCARGILL

DUNEDIN

A

A'

B

B'

C

C'

D

D'

45S

46S

167E

168E

169E

170E

109 118 108 107 117 127 106 126 116 136 105 125 115 145 104 144 135 114 154 134 124 103 123 113 143 133 102 153 132 112 162 142 122 101 152 141 131 111 161 151 121 120 110 170 130 150 140 129 119 169 160 159 149 139 138 128 171 167 157 148 147 155

Median Batholith/ Brook Street Terrane

Murihiku Terrane

Dun Mountain Ophiolite Belt

Schist

Greywacke

Cenozoic/Cretaceous sediments/volcanics

Principal faults

MT site

Figure 2.

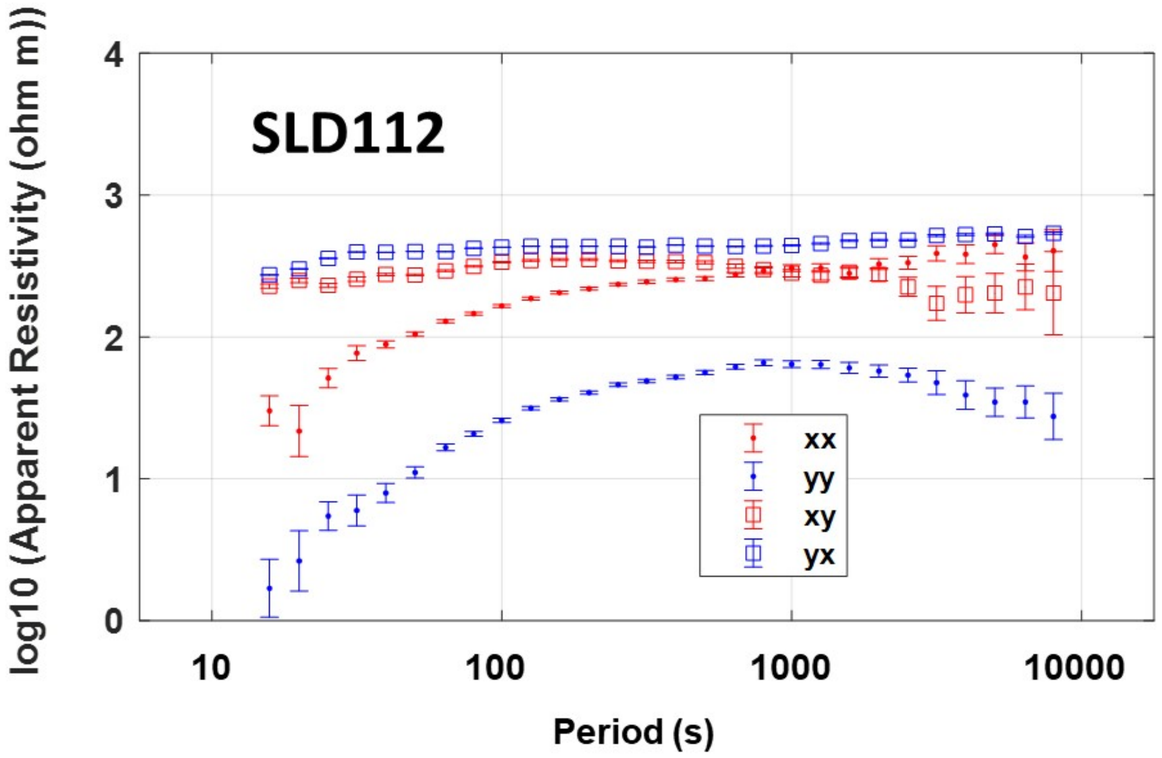
SLD112
log10 (Apparent Resistivity (ohm m))
Period (s)
xx
yy
xy
yx

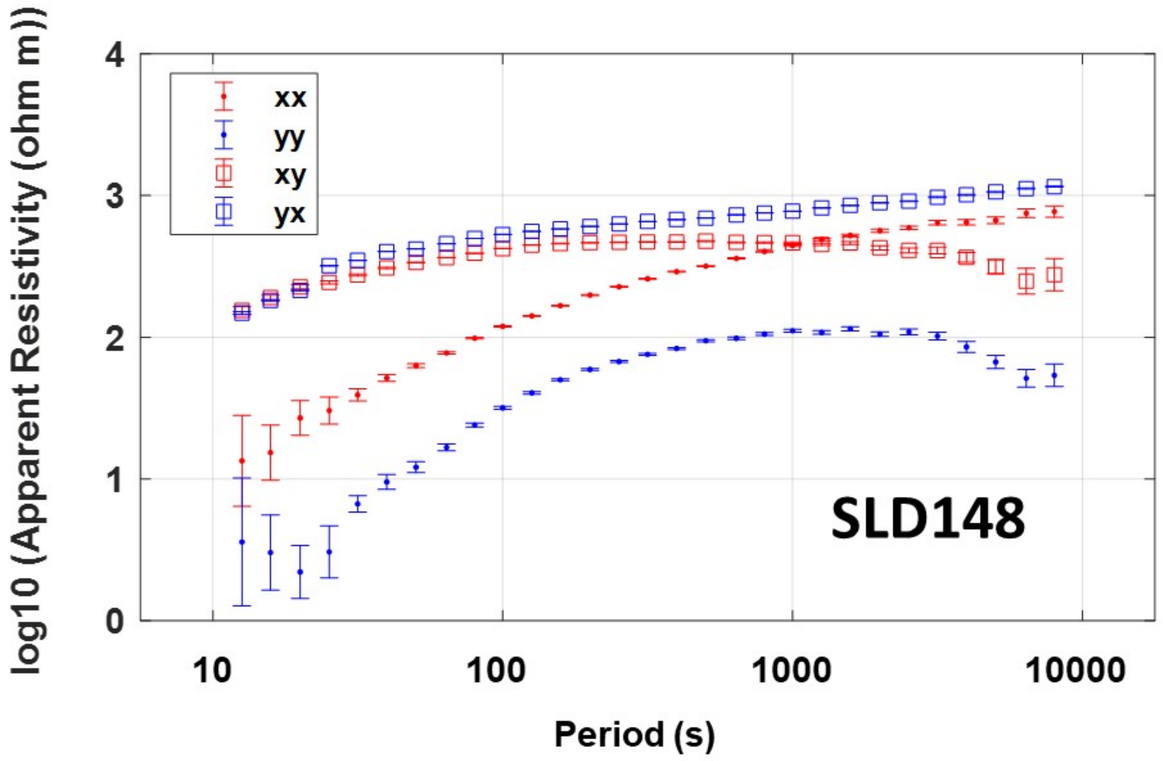
SLD148
log10 (Apparent Resistivity (ohm m))
Period (s)
xx
yy
xy
yx

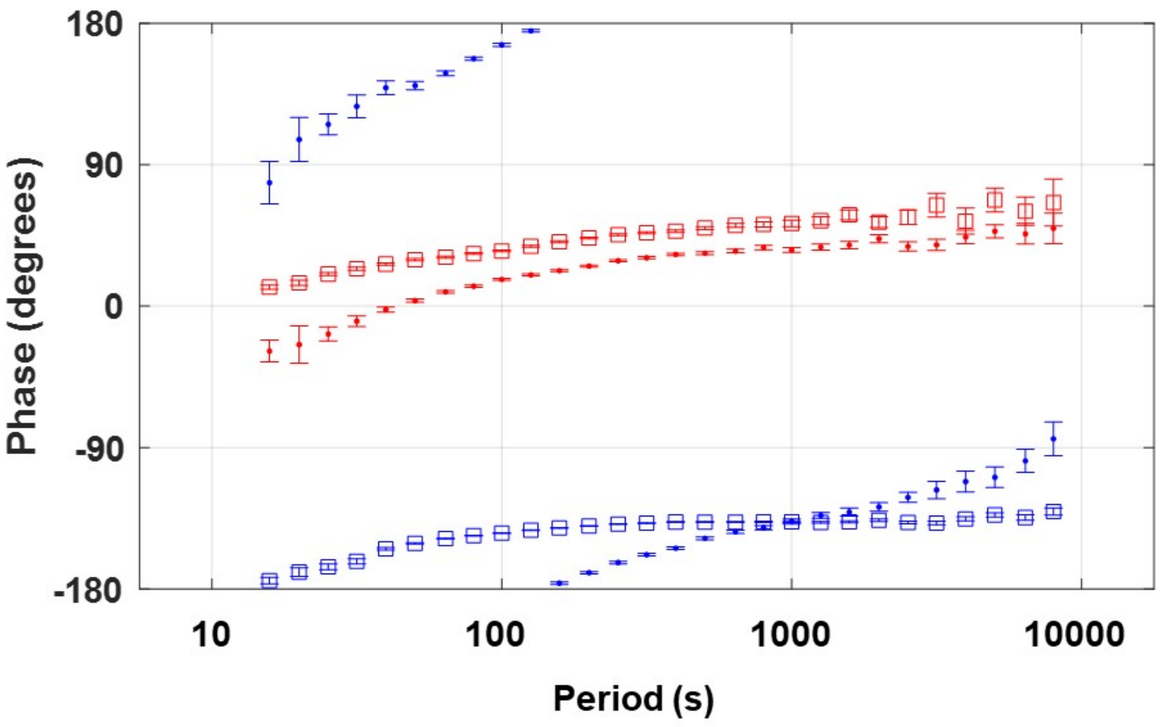
Phase (degrees)
Period (s)

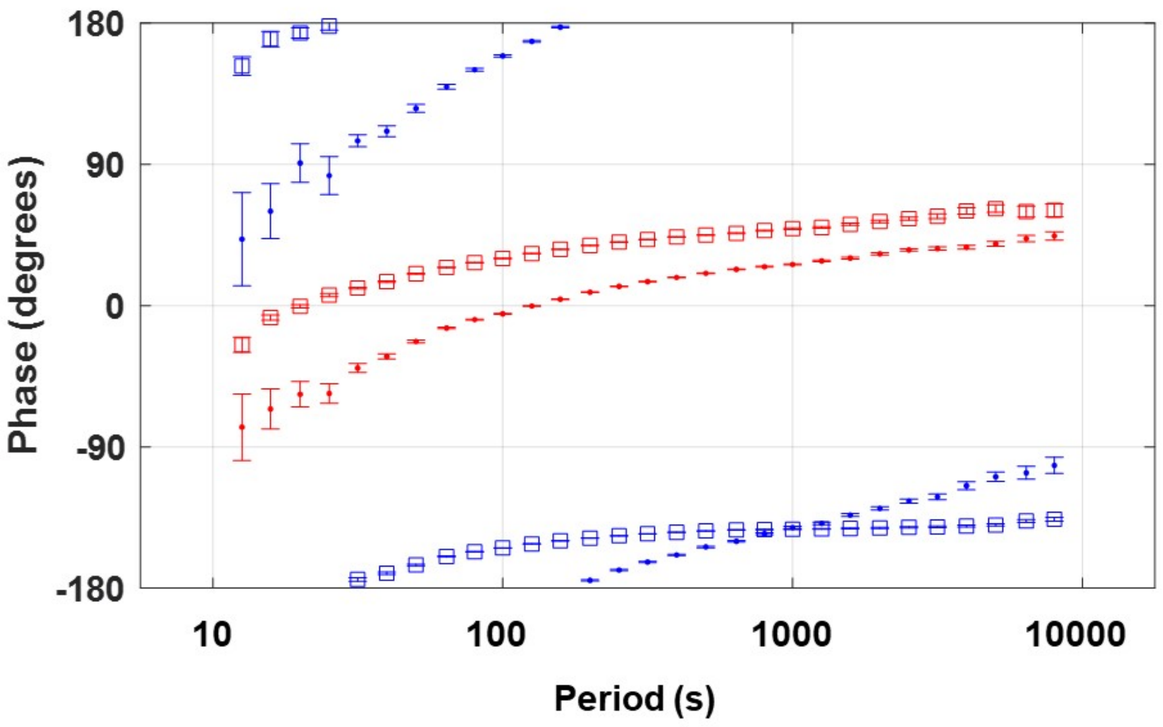
Phase (degrees)
Period (s)

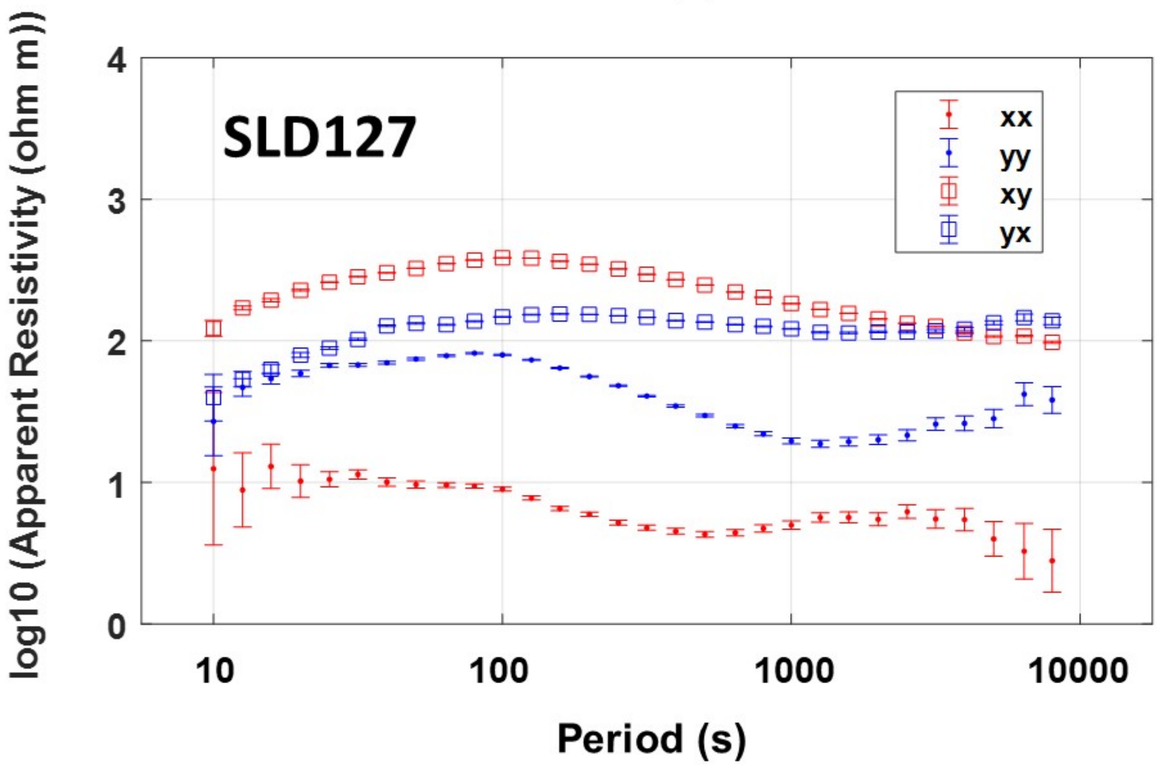
SLD127
log10 (Apparent Resistivity (ohm m))
Period (s)
xx
yy
xy
yx

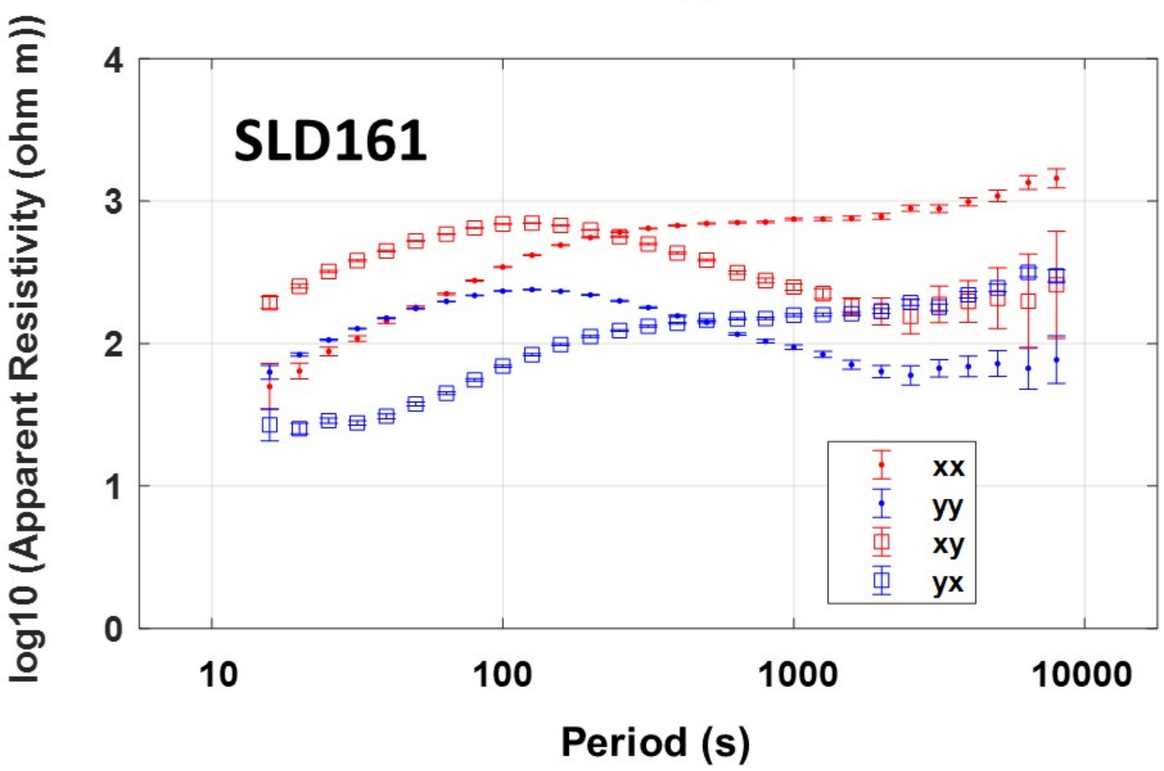
SLD161
log10 (Apparent Resistivity (ohm m))
Period (s)
xx
yy
xy
yx

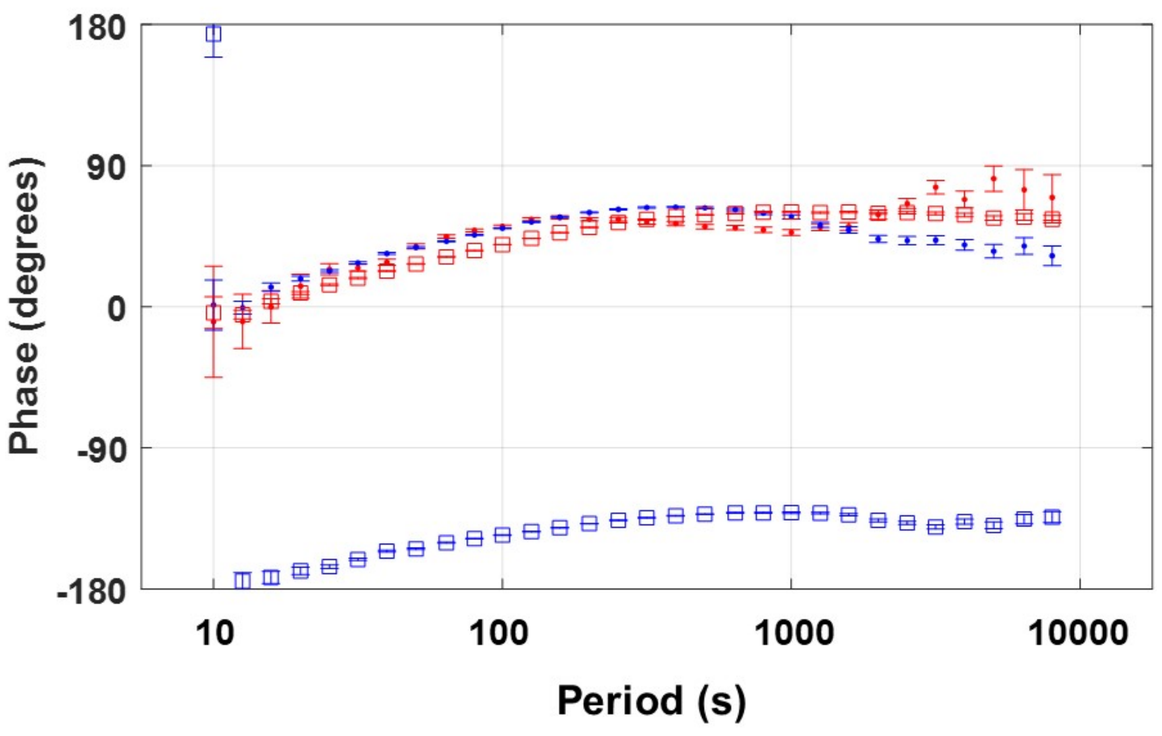
Phase (degrees)
Period (s)

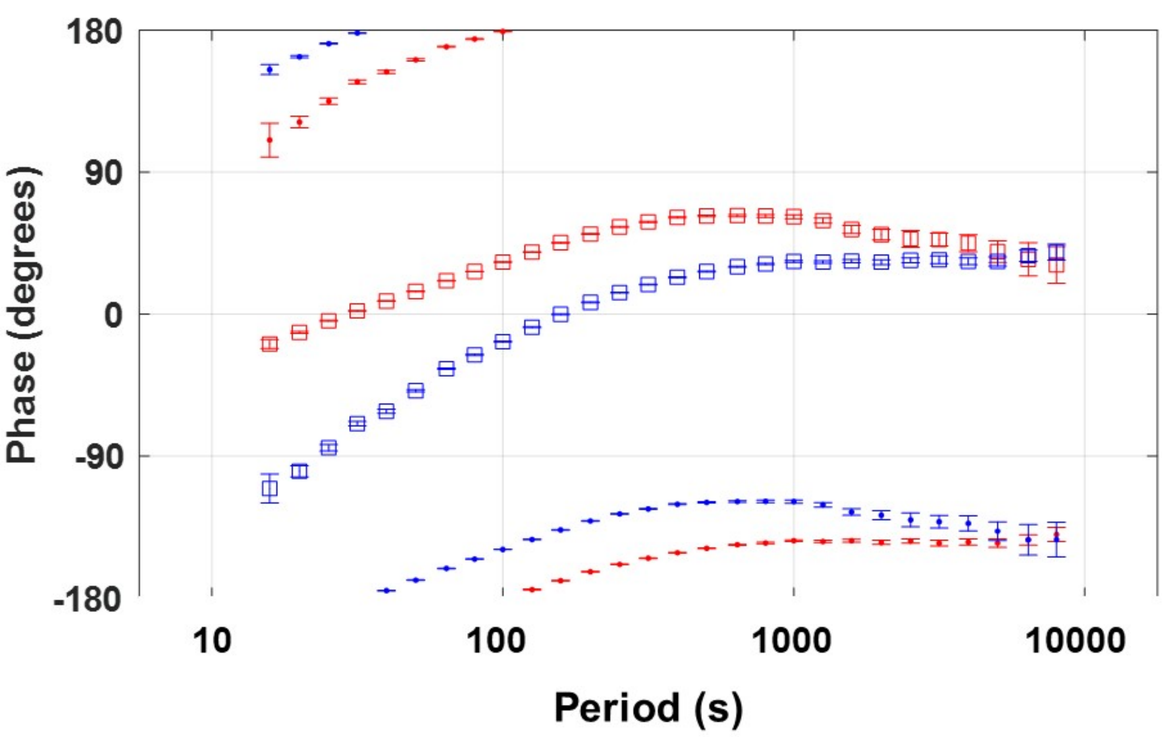
Phase (degrees)
Period (s)

Figure 3.

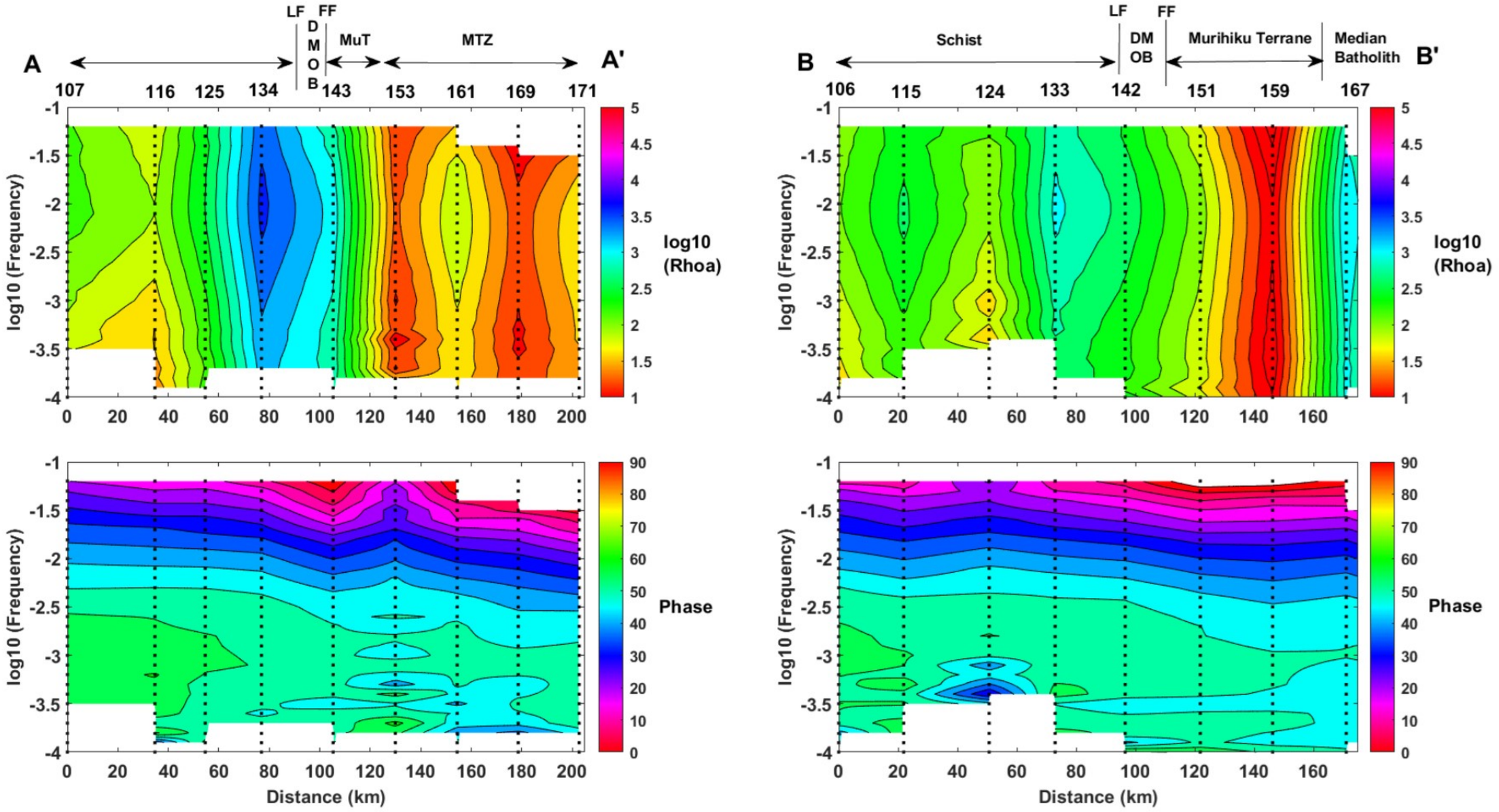
A
A'
LF
FF
DM OB
MuT
MTZ
107
116
125
134
143
153
161
169
171
B
B'
Schist
DM OB
Murihiku Terrane
Median Batholith
106
115
124
133
142
151
159
167
C
C'
105
114
123
122
131
140
149
157
D
D'
104
113
112
121
130
138
148
155
log10 (Frequency)
log10 (Rhoa)
Phase
Distance (km)

Figure 4.

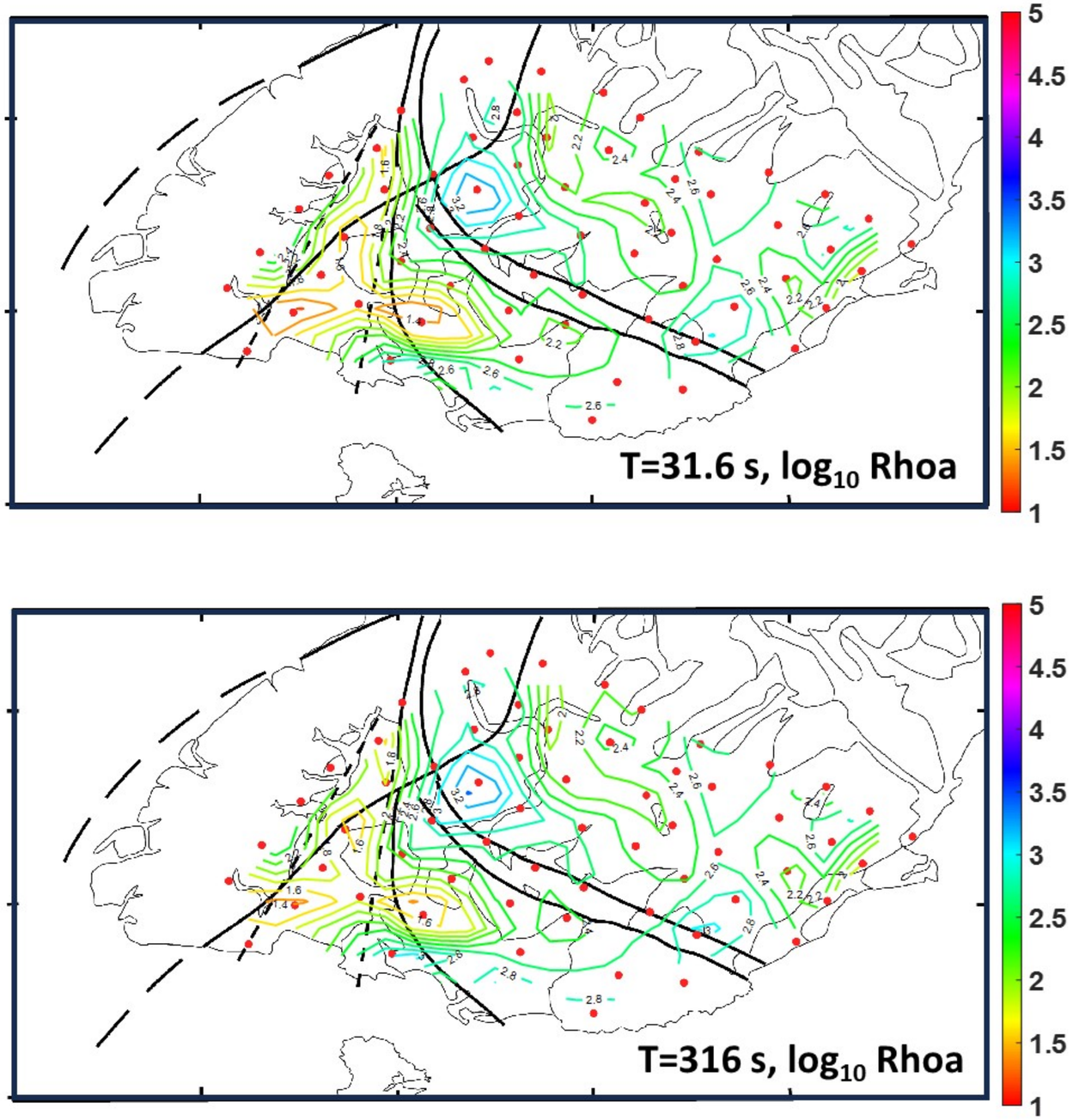
T=31.6 s, log10 Rhoa
5
4.5
4
3.5
3
2.5
2
1.5
1

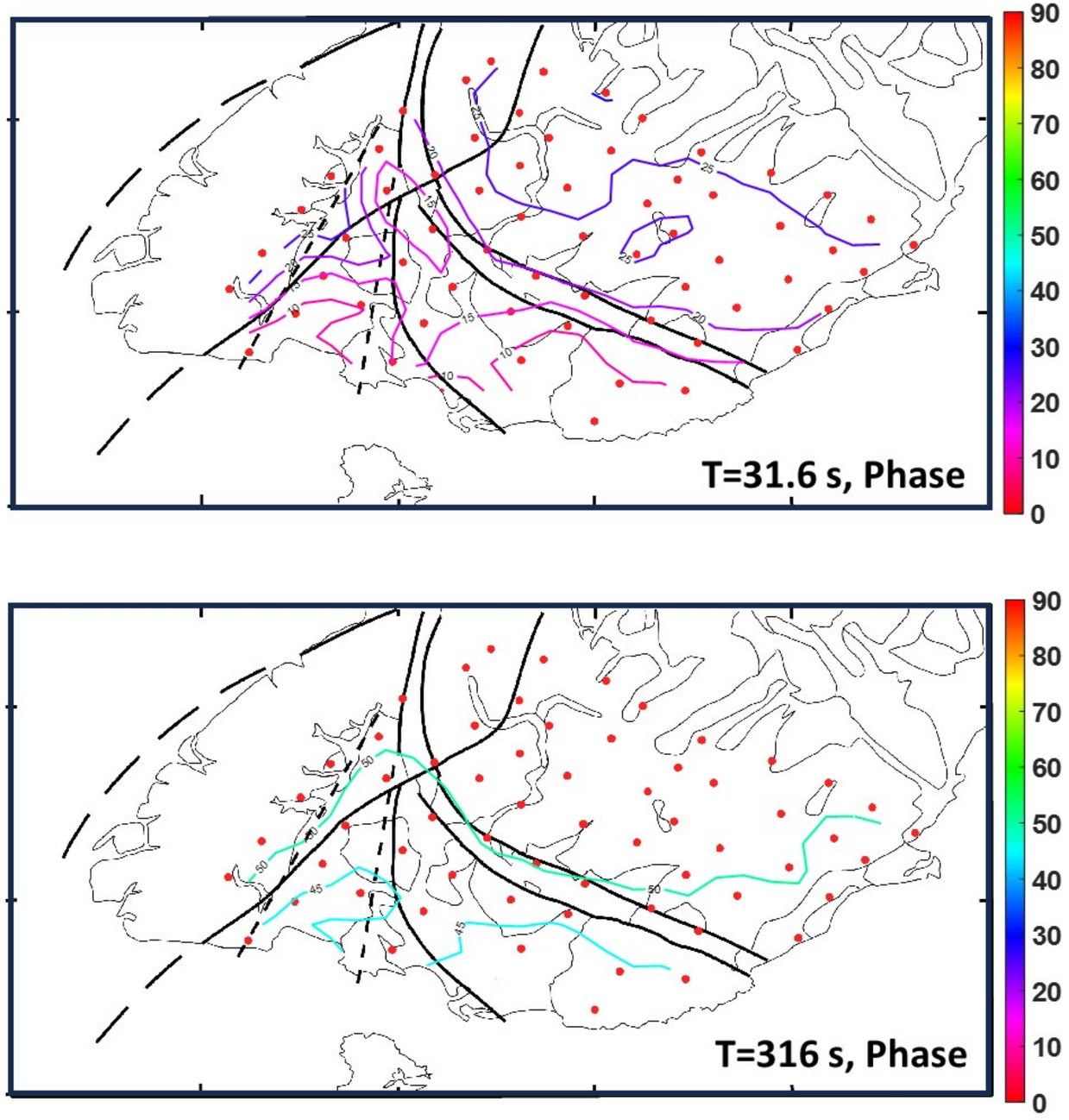
T=31.6 s, Phase
90
80
70
60
50
40
30
20
10
0

T=316 s, log10 Rhoa
5
4.5
4
3.5
3
2.5
2
1.5
1

T=316 s, Phase
90
80
70
60
50
40
30
20
10
0

T=3160 s, log10 Rhoa
5
4.5
4
3.5
3
2.5
2
1.5
1

T=3160 s, Phase
90
80
70
60
50
40
30
20
10
0

Figure 5.

Magnitude of induced E(mV/km) at T = 30s for B = 100nT N

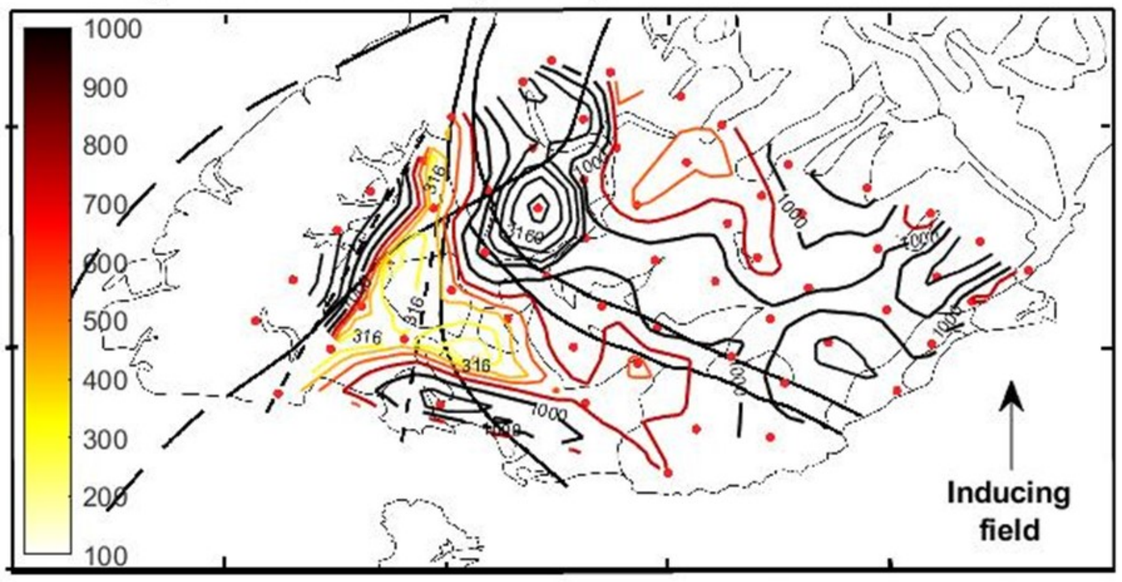

Magnitude of induced E(mV/km) at T = 30s for B = 100nT E

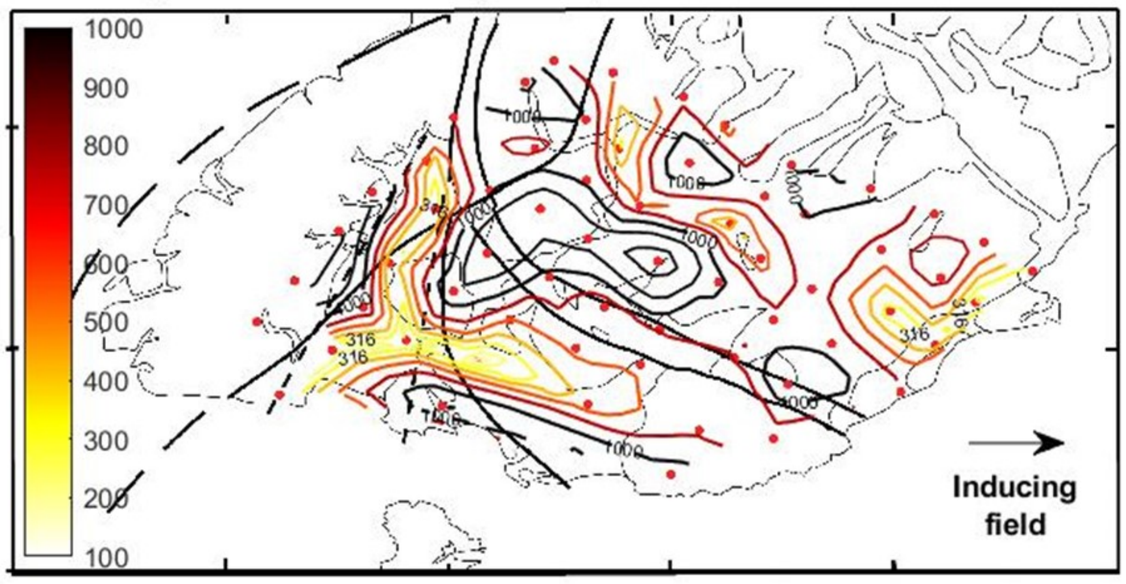

Principal axis of induced E at T = 30s for B = 100nT N

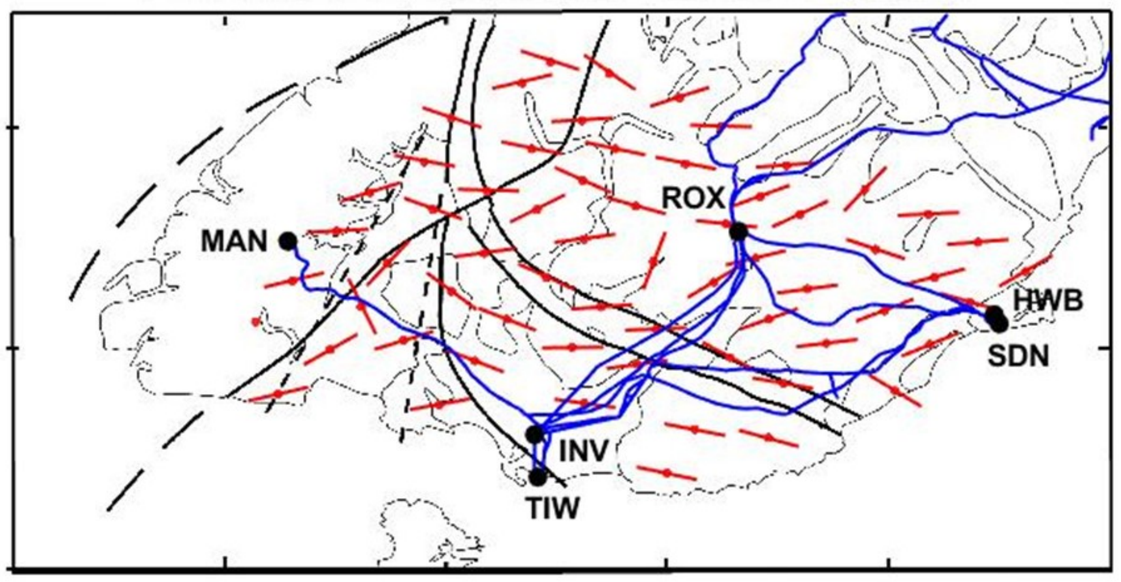

Principal axis of induced E at T = 30s for B = 100nT E

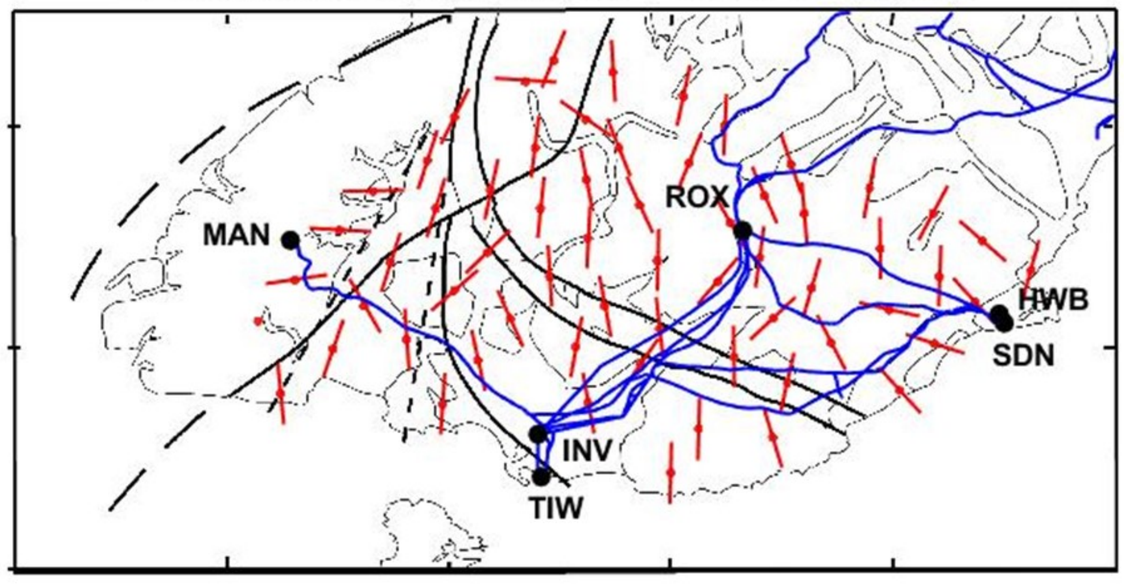

Magnitude of induced E(mV/km) at T = 30s for B = 100nT NW

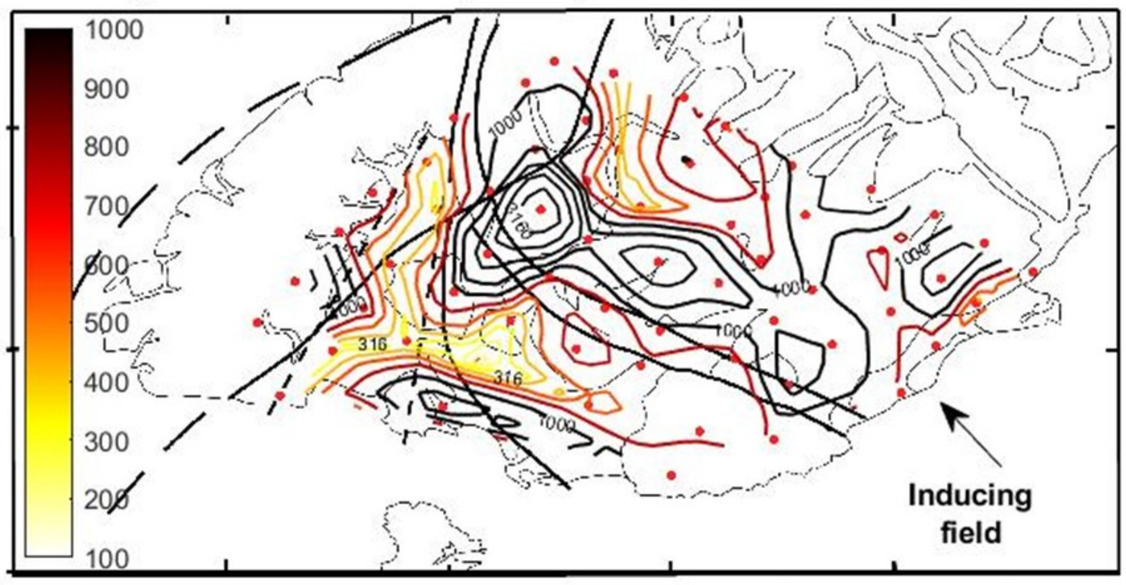

Magnitude of induced E(mV/km) at T = 30s for B = 100nT NE

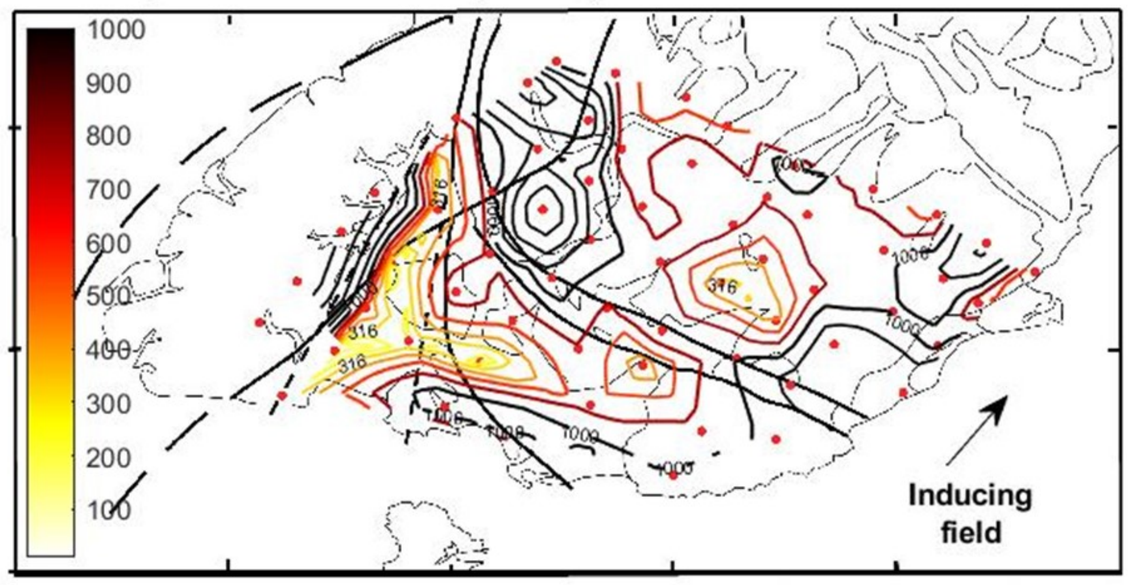

Principal axis of induced E at T = 30s for B = 100 NW

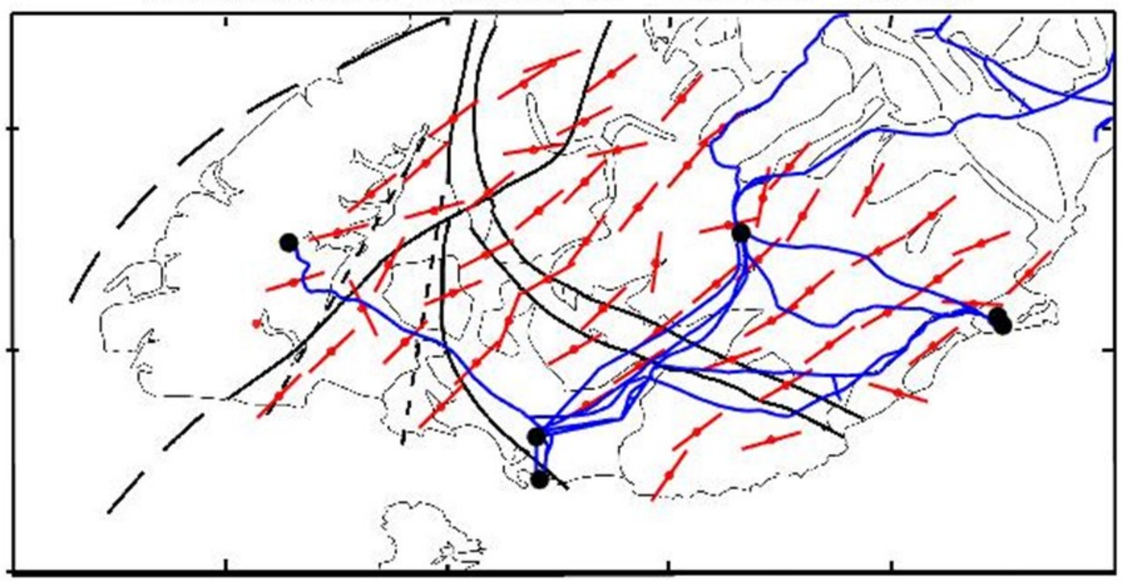

Principal axis of induced E at T = 30s for B = 100nT NE

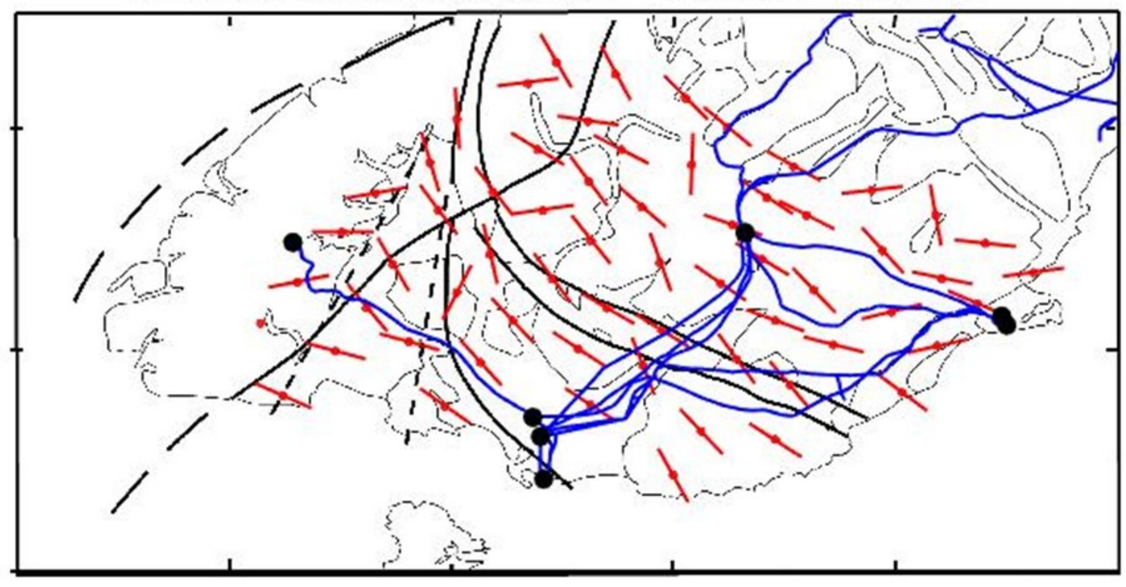

Figure 6.

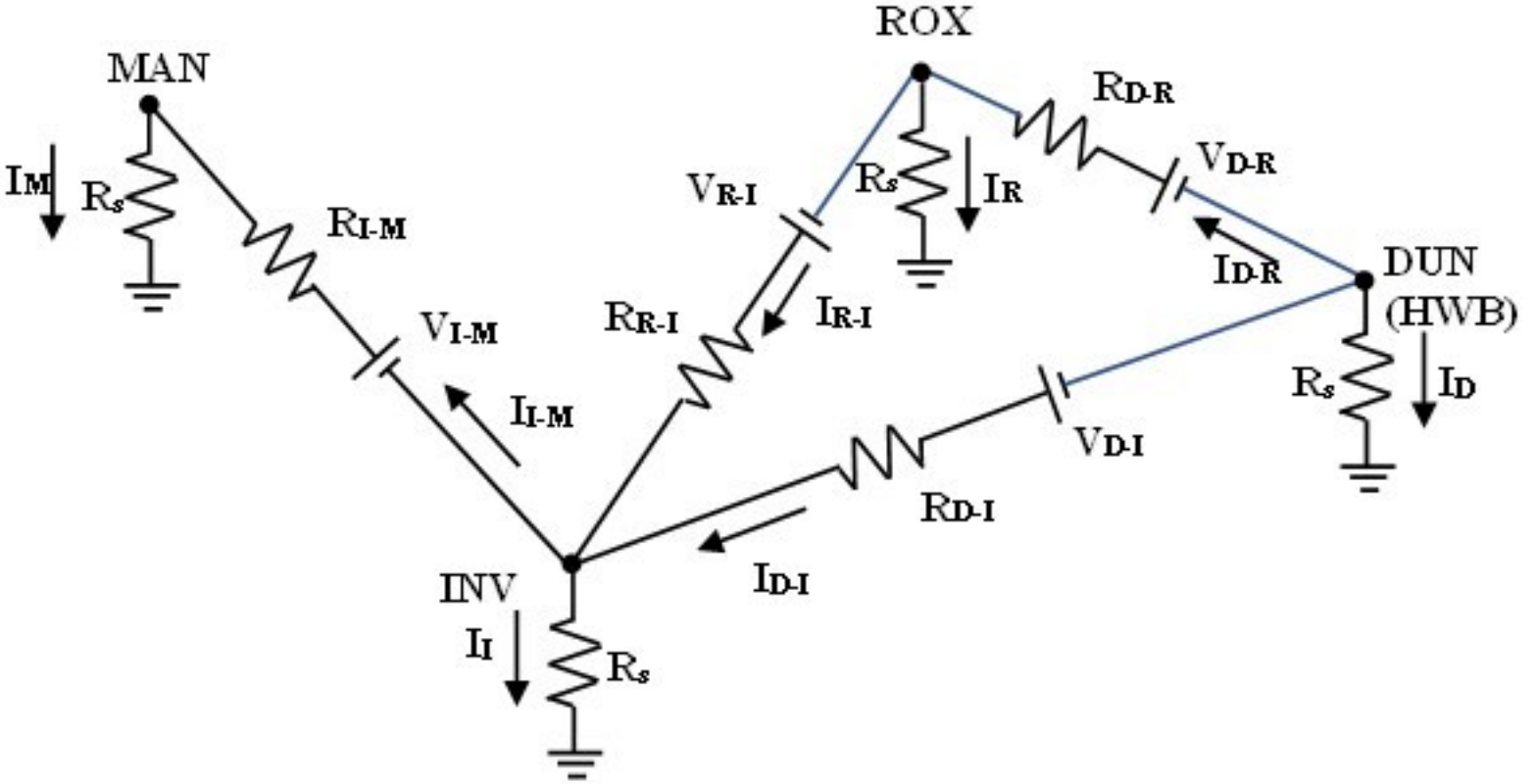
ROX
MAN
DUN
(HWB)
INV
I_M
R_s
R_{I-M}
V_{I-M}
I_{I-M}
V_{R-I}
R_{R-I}
I_{R-I}
R_s
I_R
R_{D-R}
V_{D-R}
I_{D-R}
R_s
I_D
V_{D-I}
R_{D-I}
I_{D-I}
I_I
R_s

Figure 7.

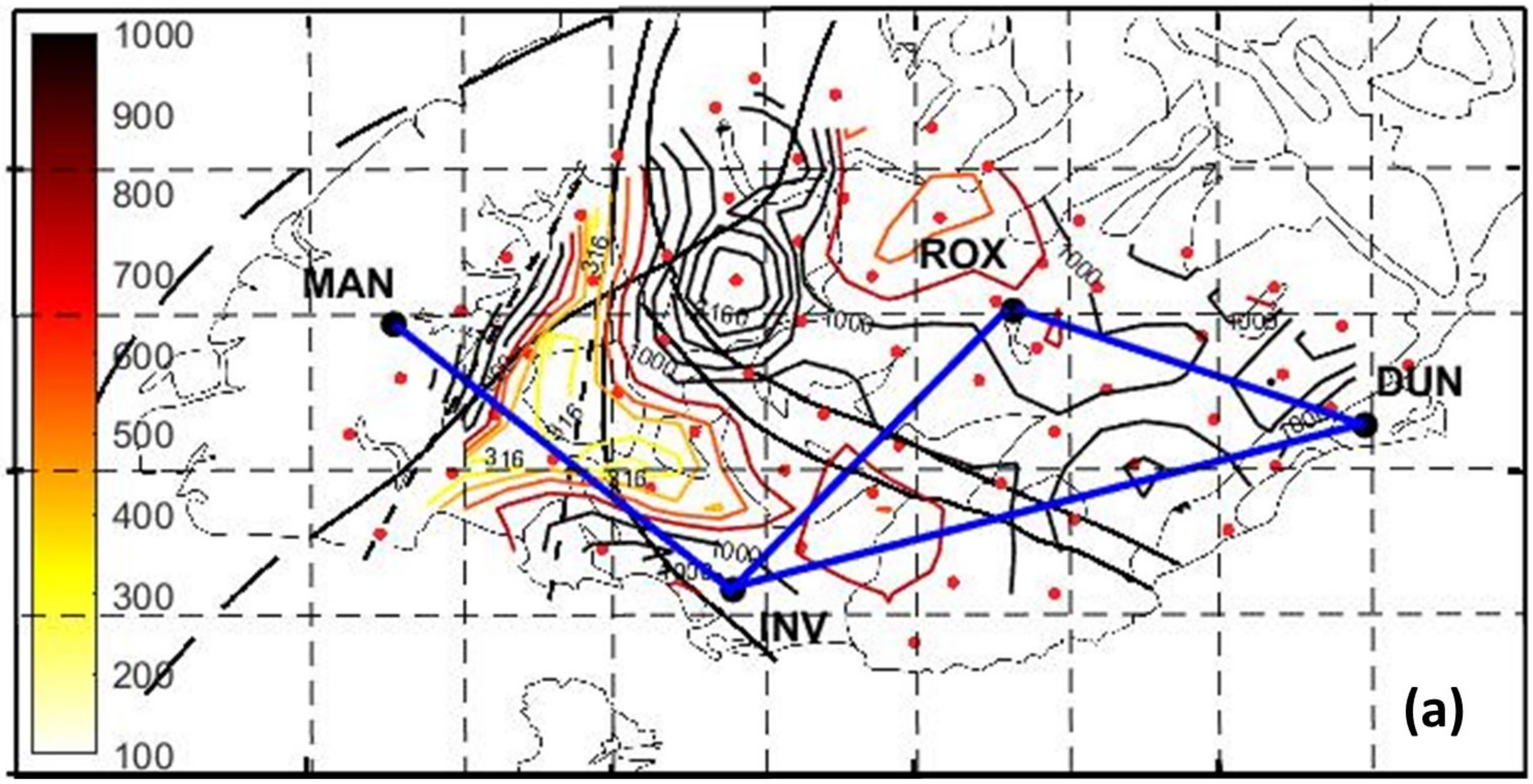
1000
900
800
700
600
500
400
300
200
100
MAN
ROX
INV
DUN
316
1000
(a)

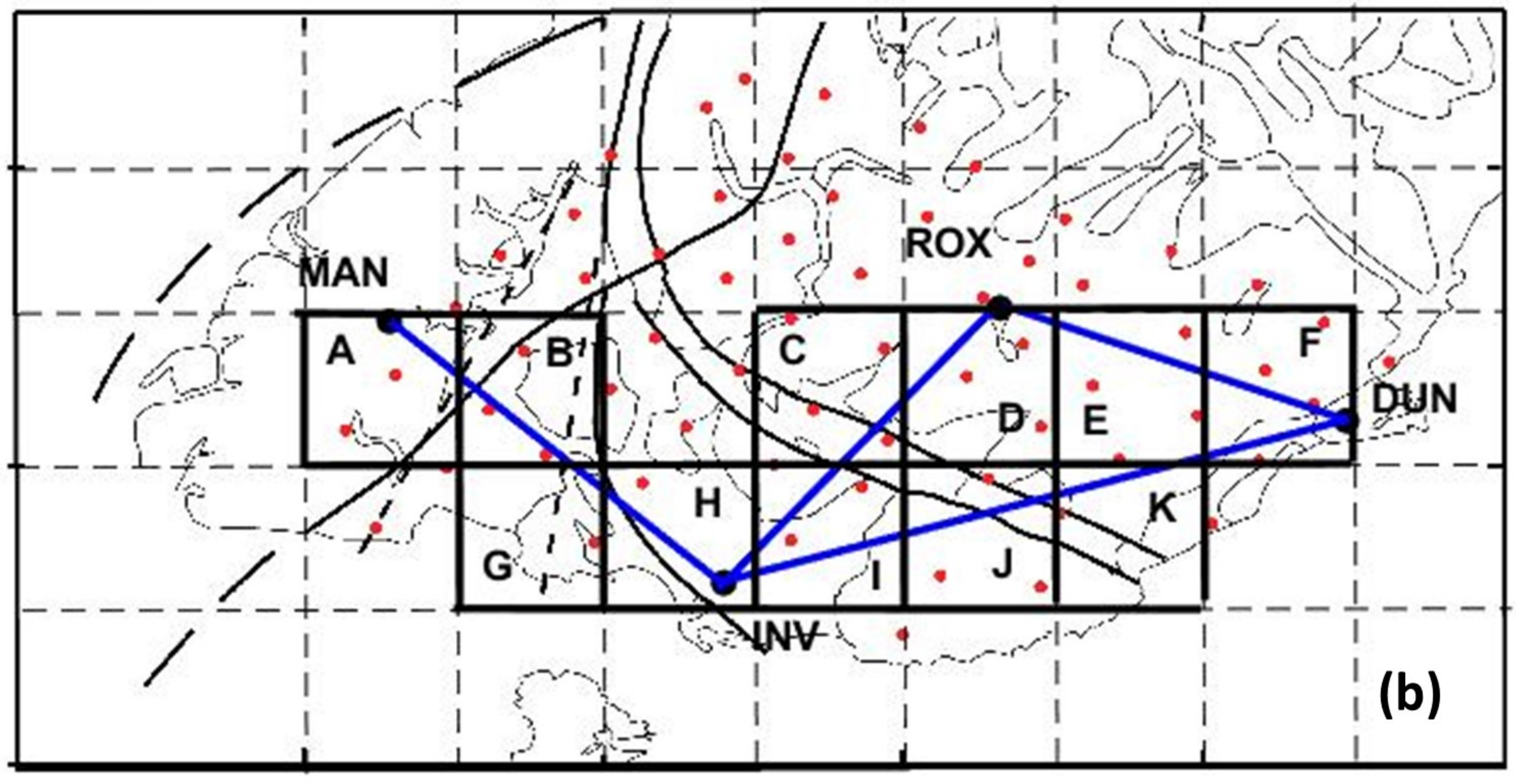
MAN
ROX
INV
DUN
A
B
C
D
E
F
G
H
I
J
K
(b)

Figure 8.

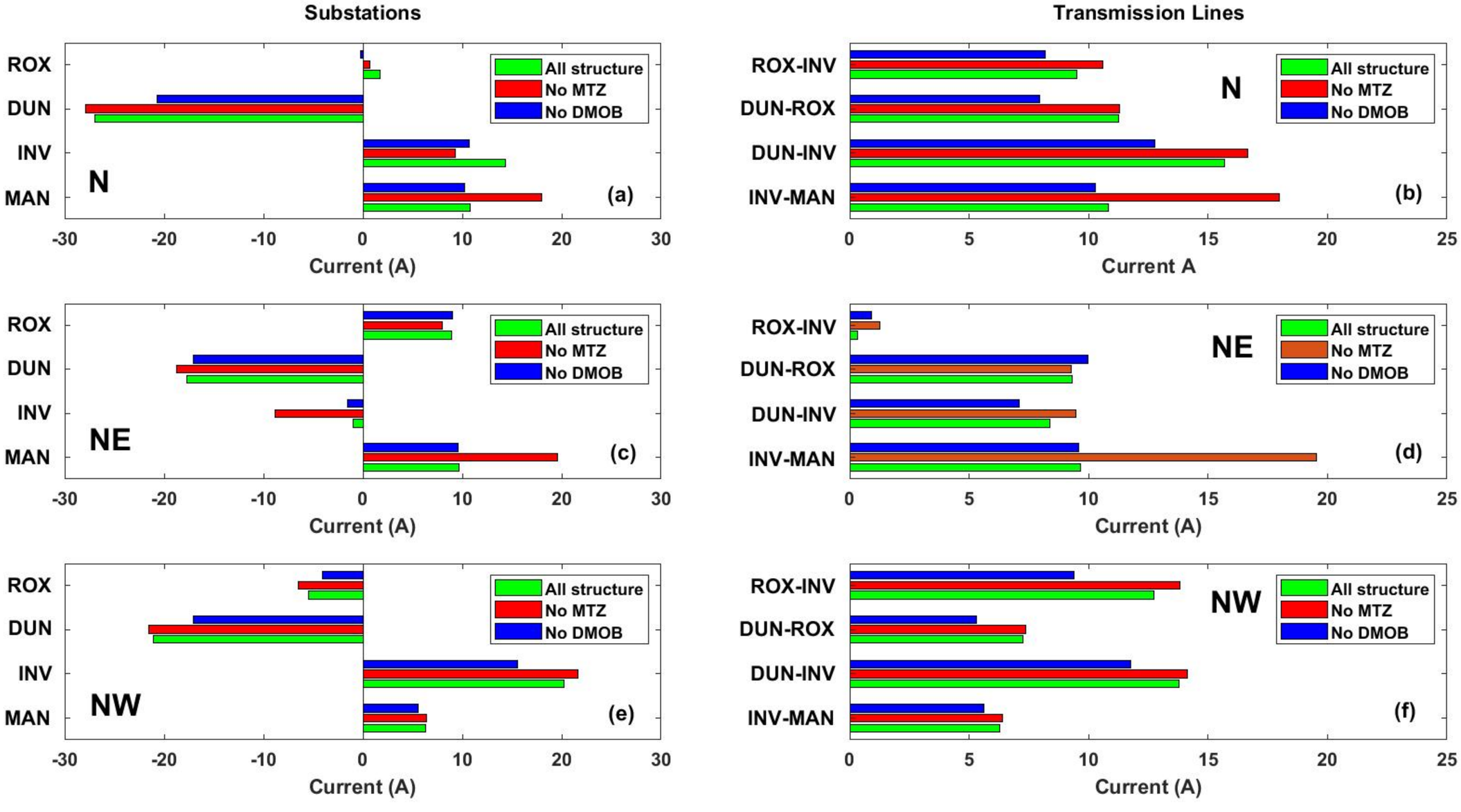
Substations
Transmission Lines
ROX
DUN
INV
MAN
N
NE
NW
All structure
No MTZ
No DMOB
(a)
(b)
(c)
(d)
(e)
(f)
-30
-20
-10
0
10
20
30
Current (A)
ROX-INV
DUN-ROX
DUN-INV
INV-MAN
0
5
10
15
20
25
Current A

Line	Length (km)	Orientation
INV - MAN	130	N42°W
DUN - INV	172	N110°W
DUN - ROX	99	N65°W
ROX - INV	124	N145°W

Table 1: Lengths and orientations of transmission lines as represented in Figure 6.

Cell	Estimated E field (mV/km)	Average electric field orientation		Cell	Estimated E field (mV/km)	Average electric field orientation
A	4417	N103°W		G	301	N100°W
B	319	N90°W		H	120	N69°W
C	1057	N111°W		I	718	N90°W
D	950	N111°W		J	965	N69°W
E	1231	N108°W		K	1589	N80°W
F	1519	N111°W				

Table 2: Average values of the magnitude and orientation of induced electric fields in each grid cell for a northward inducing field of magnitude 100 nT at period 30 s.